3-2021

A Fixed-point Method for Computing Steady-state 2D Laser-Fluid Interactions

Jeremiah S. Lane

A Fixed-Point Method for Computing Steady-State 2D Laser-Fluid Interactions

THESIS

Jeremiah S Lane, 2nd Lieutenant, USAF

AFIT-ENC-MS-21-M-002

DEPARTMENT OF THE AIR FORCE
AIR UNIVERSITY

AIR FORCE INSTITUTE OF TECHNOLOGY

Wright-Patterson Air Force Base, Ohio

AFIT-ENC-MS-21-M-002

A Fixed-Point Method for Computing Steady-State 2D Laser-Fluid Interactions

THESIS

Presented to the Faculty

Department of Mathematics and Statistics

Graduate School of Engineering and Management

Air Force Institute of Technology

Air University

Air Education and Training Command

in Partial Fulfillment of the Requirements for the

Degree of Master of Science in Applied Mathematics

Jeremiah S Lane, B.S.A.M.

2nd Lieutenant, USAF

March 25, 2021

AFIT-ENC-MS-21-M-002

A Fixed-Point Method for Computing Steady-State 2D Laser-Fluid Interactions

THESIS

Jeremiah S Lane, B.S.A.M.
2nd Lieutenant, USAF

Committee Membership:

Benjamin F Akers, Ph.D
Chair

Aihua W Wood, Ph.D
Member

Steven T Fiorino, Ph.D
Member

Maj Dana F Morrill, Ph.D
Member

AFIT-ENC-MS-21-M-002

Abstract

This research introduces a fixed-point numerical approach for solving the steady-state Navier–Stokes (NS) equations on a finite two-dimensional (2D) domain. The steady-state interaction between a high energy laser beam and its surrounding fluid medium is important to researchers in the field of high energy laser beam propagation. The solutions to the steady-state Navier–Stokes equations provide a model for uncovering the steady-state behavior of the fluid medium, which is useful for the modeling of thermal blooming in laser beam propagation. Numerical solutions remain the only tenable option for solving the NS equations, wherein numerical speed and fidelity beget the utility of any such algorithm. The timing and accuracy results from the novel fixed-point algorithm are compared to a standard Newton solver, where the fixed-point algorithm implements a series of discrete Poisson solvers through successive fixed-point iterations of fluid velocity (u,v), pressure (p), and temperature (T) in a Boussinesq fluid model. The fixed-point scheme consistently proves superior in computational cost by converging after $\mathcal{O}(N^2 \log N^2)$ flops compared to the $\mathcal{O}(N^6)$ flops in the Newton Solver for a discrete $N \times N$ grid. We provide a proof for the convergence of small amplitude solutions, and discuss the relationship between fluid parameters (Re, Ri, Pe) and the existence of solutions as a function of laser intensity in a bifurcation analysis.

Table of Contents

Page

List of Figures

Figure Page

A Fixed-Point Method for Computing Steady-State 2D Laser-Fluid Interactions

I. Introduction

In the study and application of fluid dynamics within the domain of engineering and applied physics, the solutions to the Navier–Stokes (NS) equations remain a topic of pressing research interest. The solutions to these equations fundamentally describe the spatial and temporal behavior of a fluid model within a specified domain. Beyond the immediate utility of being able to describe the dynamics of a fluid model, such an understanding proves useful for the determination of high energy laser behavior through fluids. Specifically, the physical phenomenon of thermal blooming remains a pertinent research interest in applied physics. This research requires a suitable comprehension of the manner in which heat energy from a laser interacts with the dynamics of the surrounding fluid medium. The steady-state behavior is of particular interest, wherein the fluid dynamics remain fixed in time for a specific laser heating profile. In this research, we seek to develop a numerical approach to solving the steady state case of the NS equations on a finite two-dimensional domain under a Boussinseq fluid model. Such a solution will output the state variables pressure (p), temperature (T), and velocity (u, v) relative to the local atmosphere of the domain.

1.1 Problem Motivation

1.1.1 Laser Propagation

For years, researchers in the field of high-energy laser (HEL) beam propagation have been concerned with developing a systematic understanding of the interaction

between the laser and its propagating medium [1]. Such interactions tend to prove detrimental to laser performance, as they lead to laser wavefront degradation and an overall decrease of energy available to the target site. When one is concerned with optimizing accuracy and efficiency while operating a high energy laser, this manifests as a problem of preeminent importance. We now delineate laser interactions within the surrounding atmosphere into three distinct yet interrelated phenomena: atmospheric turbulence, thermal blooming, and molecular absorption.

Atmospheric turbulence refers to the stochastic fluctuation of the constituent air's temperature, leading to fluctuations in its refractive index [2]. Current physical models exist which statistically treat these fluctuations using frequency-based methods [3]. A thorough understanding of these models is especially necessary for applications in which HEL's propagate over long distances such that the turbulent nature of the refractive index fluctuations accumulate over spatial propagation length. It is important to understand that this turbulence is an inherent property of the atmosphere which is not induced by the laser. As such, atmospheric turbulence is treated separately from the other two interaction categories since its impact on laser beam propagation is not explicitly dependent on the intensity of the laser.

Divergently, thermal blooming and molecular absorption are of particular interest to this research as they require acute investigation of the physical interaction between the HEL and the atmosphere. Thermal blooming occurs when the laser energy is absorbed by the air, leading to an increase in local temperature and a subsequent decrease in local air density [4]. Like the temperature fluctuations described by atmospheric turbulence, this results in a shift of the refractive index of the laser along its atmospheric path. The accumulated shifts in refractive index then result in wavefront defocusing and aberrational movement in beam location. Eventually, the effects of thermal blooming and atmospheric turbulence on laser beam propagation

may equilibrate into a steady-state. Analysis in thermal blooming assumes a continuum model of air such that discrete interactions between the laser and individual air molecules are ignored. Such analysis can be implemented through the Navier-Stokes equations equipped with a sufficient model for local atmospheric air. Consideration of molecular absorption then takes this approach a step further and accounts for energy absorption at discrete molecular wavelengths. For most atmospheric regimes, the continuum approach proves sufficient due to the lack of polarity and distinct absorption characteristics amongst air molecules [5]. In environments with significant aerosol presence, however, excitation of the rotational and vibrational modes of the aerosol particles may induce significant enough changes to the index of refraction such that a continuum approach proves insufficient. Figure 1 provides a pictorial representation of the effects of thermal blooming on the laser wavefront.

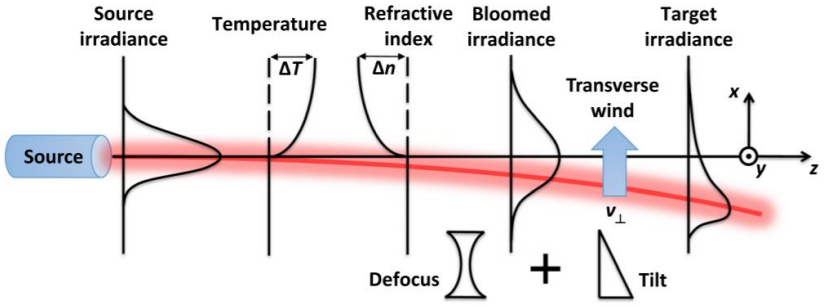

Figure 1: Visual depiction of the impact of thermal blooming on the laser wavefront due to changes in refractive index caused by temperature variations. This representation includes a transverse wind acting on the propagating beam, which induces a tilting effect such that the peak irradiance shifts off-center. Taken from Spencer [6].

In time dependent simulations of laser beam propagation, the cumulative effects of each of these modes of beam distortion require an intensive treatment of both statistical and deterministic models for laser-fluid interaction [7]. As such, this research will instead focus solely on the steady-state behavior of the fluid surrounding the laser.

This approach grants a viable methodology for determining whether such solutions exist, and if so, allows us to model fluid behavior as a function of only the domain and the steady laser forcing. With an explicit determination of the fluid behavior in a steady-state regime, one may then establish a model for laser beam propagation over a long period of time while accounting for thermal blooming.

1.1.2 Fluid Modeling

To determine the steady-state behavior of the laser's fluid medium, we must determine an appropriate fluid model which accurately explicates its thermal interaction with the laser in a 2D domain. This is done almost universally by modeling the fluid through the Navier–Stokes equations, upon which certain assumptions and simplifications are imposed based on the fluid and domain properties. While solutions determined from these equations are preeminently accurate for modeling fluid behavior, exact, analytic solutions remain elusive apart from some primitive problems with necessarily favorable fluid and domain properties. The problem of determining the nature of analytical solutions to the NS equations remains so pressing that a proof for the existence of smooth solutions in a general 3D problem is one of the current Millennial Prize problems in mathematics [8]. The field of computational fluid dynamics (CFD) thus arises as a response to the ubiquity of fluid modeling in applied science and the necessity of computing numerical solutions to the NS equations.

In the pursuit of a steady-state fluid model which interacts with a laser beam, we hence seek to develop a sufficient CFD model for computing these solutions. In any venture in computational mathematics, it is important to characterize the numerical properties of any algorithmic approach to solving a problem. The most prominent properties of interest include numerical accuracy, stability, and computational time for a given numerical solver [9]. Contemporary CFD methods utilize various numerical

approaches to discretize the domain and to solve the governing equations over this domain. The method selected for computation will be based on the size and resolution of the discretized domain, the desired accuracy of the numerical solution, and the desired timescale for computation. While modern CFD approaches are greatly useful for dealing with complex domain geometry, there continues to be research opportunity for optimizing numerical solvers in time for more facile geometries. For example, Ahmad [10] explores the computation of steady-state Navier–Stokes equations over a horizontal cylinder with an adaptive grid in a finite-difference iterative scheme. Dennis, Hudson, and Smith [11] compute steady, forced convection over a similar geometry by converting the governing equations to a system of odes in a stream function formulation and solving them numerically. Deparis and Rozza [12] introduce a reduced basis approach coupled with an iterative scheme on rectangular cavities for solving the steady Navier–Stokes equations. With respect to laser-fluid interaction dynamics, Livingston [13] treats fluid convection through a geometric optics approach and Flores–Flores et. al. [14] considers a finite element approach to manipulating microparticles in convective currents. While research involving the physics of laser-fluid interaction is well developed, the conventional numerical approaches used to solve the governing equations are often expensive in computational time. Therefore, we seek to develop a numerical approach which markedly reduces computational cost for an equivalent numerical fidelity in a laser-fluid interaction problem over a simple domain geometry.

1.2 Research Objectives

As mentioned above, we seek to elucidate our approach to developing a novel numerical solver which outperforms contemporary numerical algorithms for the modeling of a thermal laser-fluid interaction in a 2D domain. Our research objectives thus

manifest in a twofold manner:

1. Numerical analysis:
   (a) introduce fixed-point numerical algorithm to solving steady-state NS equations for classical boundary conditions over a finite, rectangular domain,
   (b) prove that steady-state solutions exist and that the proposed algorithm converges for small amplitude laser forcing,
   (c) validate theoretical convergence analysis with numerical convergence results,
   (d) confirm the reduced computational cost of this approach relative to a conventional Newton solver,
   (e) provide functional code implementing the algorithm for different classical boundary conditions and laser forcing amplitudes.
2. Physical interpretation:
   (a) develop a laser-fluid model which accurately depicts steady-state thermal blooming in a 2D domain,
   (b) determine boundary conditions and produce a solution which accurately represents an experimental laser setup in a finite box,
   (c) provide a practical methodology for utilizing the numerical algorithm in future laser beam propagation research.

1.3 Document Overview

The following chapters will describe the problem development, relevant research background, solution methodology, and results and analysis of the findings. Consideration of the problem domain, boundary conditions, and numerical fidelity will become

paramount as we elucidate the procedure for arriving at the desired solution method. We will then introduce key mathematical ideas culminating in a proof of convergence of solutions with our fixed-point method. We then validate this convergence analysis by comparing the theoretical maximum laser amplitude to numerical results. Following this study, we present solution profiles of the steady-state variables (p, T, u, v) for various boundary conditions and we introduce a bifurcation analysis which describes the existence of convergent solutions as a function of laser forcing amplitude. After a sufficient discussion of these findings, we will then explore future avenues of research which build upon our findings in the pursuit of more effective laser-fluid models and their associated solution methodologies.

II. Problem Development

In this chapter, we introduce the foundational aspects of our approach to mathematically describing the laser-fluid interaction of interest. We summarize the equations governing fluid behavior within our specified domain and justify their propriety on the basis of certain assumptions on fluid properties. In relating this mathematical model to the physical problem, we discuss the possible formulations of the boundary conditions imposed on the fluid variables and their necessary implications on the fluid dynamics. With the modeled problem suitably developed, we then explore several approaches for determining solutions.

2.1 Governing Fluid Model

2.1.1 Domain and Governing Equations

As described in Chapter I, we seek to develop a model for laser-fluid interaction on a finite, 2D domain such that this domain can be thought of as a rectangular cross section of the propagation path of the laser beam. That is, the domain will be a rectangular subsection of the xy plane as defined in Figure 1 where we assume the laser is centered on the origin of the domain. In this case, the laser forcing is also 2D where we assume a Gaussian profile about the origin. We denote the domain as Ω and the boundary of the domain as $\partial\Omega$, where we begin by considering a unit square domain $\Omega = [-0.5, 0.5] \times [-0.5, 0.5]$. Figure 2 depicts the domain and coordinate system used for the remainder of our analysis.

With the domain established, we now introduce several assumptions on the fluid and laser properties in the pursuit of governing equations which dictate fluid behavior. These assumptions are enumerated as follows:

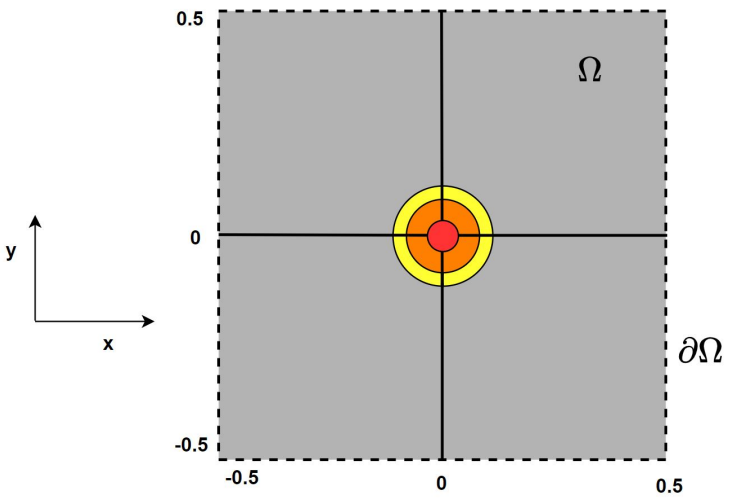

Figure 2: Visualization of the fluid boundary and domain with laser forcing centered on the origin. Both the x and y coordinates range from -0.5 to 0.5.

1. The fluid within the domain is Newtonian: that is, the fluid follows Newton's law of viscosity and we may express its conservation of mass and momentum through the Navier–Stokes equations.

2. The fluid is incompressible: we assume that variations in fluid pressure due to temperature fluctuations do not result in density variations. This is described by zero velocity divergence in the equation $\nabla \cdot \mathbf{u} = 0$ for some velocity field $\mathbf{u}$ of the fluid.

3. The fluid dynamics follow a buoyancy-driven, Boussinesq approximation: variations in fluid density have a linear relationship with temperature. This is a common assumption for fluids which are driven by internal temperature variations. A more thorough discussion on the validity and derivation of the Navier–Stokes equations for incompressible, Boussinesq flows is provided in Morrill [15].

4. Temperature as a function of laser irradiance: we may represent the normalized laser irradiance as a function defined over the domain Ω such that the laser

heats the fluid and induces temperature variations.

With the necessary assumptions properly elucidated, we now introduce the governing equations for the problem at hand. We seek functions

$$T : \Omega \to \mathbb{R}, \quad p : \Omega \to \mathbb{R} \quad \mathbf{u} : \Omega \to \mathbb{R}^2$$

representing the nondimensional temperature, pressure, and velocity field of the fluid which obey the incompressible, Boussinesq Navier–Stokes equations undergoing forcing:

$$\begin{aligned} \mathbf{u}_t + (\mathbf{u} \cdot \nabla)\mathbf{u} &= \nabla p + \frac{1}{Re}\Delta \mathbf{u} + RiT\mathbf{e_2}, && \text{(1a)} \\ \nabla \cdot \mathbf{u} &= 0, && \text{(1b)} \\ T_t + (\mathbf{u} \cdot \nabla)T &= \frac{1}{Pe}\Delta T + F, && \text{(1c)} \end{aligned}$$

where $F : \Omega \to \mathbb{R}$ represents the laser forcing and $\mathbf{e_2}$ represents the unit vector in the y direction as depicted in Figure 2. In this representation, we utilize the notation $\Delta = \nabla \cdot \nabla = \nabla^2$ and the constants Re, Ri, Pe denote the flow Reynolds number, Richardson number, and Peclet number, respectively. We seek steady-state solutions such that all temporal variation is negligible and each $\mathbf{u}_t = T_t = p_t = 0$, where the incompressibility condition can be equivalently expressed in the equations (2) as derived in [15]:

$$\begin{aligned} (\mathbf{u} \cdot \nabla)\mathbf{u} &= \nabla p + \frac{1}{Re}\Delta \mathbf{u} + RiTe_2, && \text{(2a)} \\ \nabla \cdot (\mathbf{u} \cdot \nabla)\mathbf{u} &= \Delta p + \nabla \cdot (RiT\mathbf{e_2}), && \text{(2b)} \\ (\mathbf{u} \cdot \nabla)T &= \frac{1}{Pe}\Delta T + F. && \text{(2c)} \end{aligned}$$

With the governing equations explicated, we now apply boundary conditions to the

domain such that the problem achieves a unique solution for a determined laser forcing function.

2.1.2 Boundary Conditions

By observing the form of the system of equations (2), we may interpret the system as a type of vector-valued, nonlinear Poisson equation over the domain Ω. Letting $\boldsymbol{\varphi} = [T, p, \mathbf{u}]^\intercal$, the nonlinear Poisson formulation of (2) takes the form

$$\Delta\boldsymbol{\varphi} = \mathbf{f}(D^2\boldsymbol{\varphi}, D\boldsymbol{\varphi}, \boldsymbol{\varphi}, F) \tag{3}$$

for some vector-valued function $\mathbf{f}$ of the derivatives of $\boldsymbol{\varphi}$ and the laser forcing F. By defining the velocity vector field $\mathbf{u} = [u, v]^\intercal$, we write the vector valued equation (3) explicitly as the following system of scalar equations

$$\begin{aligned}
\Delta u &= Re\left((\mathbf{u}\cdot\nabla)u - p_x\right), && \text{(4a)}\\
\Delta v &= Re\left((\mathbf{u}\cdot\nabla)v - p_y - RiT\right), && \text{(4b)}\\
\Delta p &= \nabla\cdot(\mathbf{u}\cdot\nabla)\mathbf{u} - RiT_y, && \text{(4c)}\\
\Delta T &= Pe\left((\mathbf{u}\cdot\nabla)T - F\right). && \text{(4d)}
\end{aligned}$$

These equations represent a coupled, second order, quasilinear system of partial differential equations defined over a 2D domain. Significant research in applied mathematics has been devoted to the classification of, and the study of the existence and uniqueness of solutions to, such systems partial differential equations. For further treatment of the analysis of second order pdes, see Colton [16]. We now introduce boundary conditions and consider the boundary value problem defined on $\Omega \subset \mathbb{R}^2$ where by the Heine–Borel theorem we note that Ω is compact due to its being a closed and bounded subset of $\mathbb{R}^2$. We consider the classical boundary value problems for an

elliptic, second order pde where we initially seek strong form solutions $\varphi_j \in C^2(\Omega)$ for each fluid variable $\varphi_j(x,y) \in \boldsymbol{\varphi}$ defined in equation (3). These classical boundary value problems are distinguished as follows:

1. Dirichlet condition: find $\varphi_j \in C^2(\Omega)$ such that for some $g_j(x,y) \in C^2(\Omega)$:

$$\begin{cases} \Delta\varphi_j = f_j(D^2\boldsymbol{\varphi}, D\boldsymbol{\varphi}, \boldsymbol{\varphi}, F), & (x,y) \in \Omega \\ \varphi_j = g_j(x,y), & (x,y) \in \partial\Omega. \end{cases} \tag{5}$$

2. Neumann condition: find $\varphi_j \in C^2(\Omega)$ such that for the unit outward normal vector $\mathbf{n}$ to $\partial\Omega$ and some $h_j(x,y) \in C^1(\Omega)$:

$$\begin{cases} \Delta\varphi_j = f_j(D^2\boldsymbol{\varphi}, D\boldsymbol{\varphi}, \boldsymbol{\varphi}, F), & (x,y) \in \Omega \\ \frac{\partial\varphi_j}{\partial\mathbf{n}} = h_j(x,y), & (x,y) \in \partial\Omega. \end{cases} \tag{6}$$

3. Mixed condition: Let the boundary be a union of disjoint sets $\partial\Omega = \partial\Omega_D \cup \partial\Omega_N$. Find $\varphi_j \in C^2(\Omega)$ such that for the unit outward normal vector $\mathbf{n}$ to $\partial\Omega$ and some $g_j(x,y) \in C^2(\Omega)$ and $h_j(x,y) \in C^1(\Omega)$:

$$\begin{cases} \Delta\varphi_j = f_j(D^2\boldsymbol{\varphi}, D\boldsymbol{\varphi}, \boldsymbol{\varphi}, F), & (x,y) \in \Omega \\ \varphi_j = g_j(x,y), & (x,y) \in \partial\Omega_D \\ \frac{\partial\varphi_j}{\partial\mathbf{n}} = h_j(x,y), & (x,y) \in \partial\Omega_N. \end{cases} \tag{7}$$

In colloquial terms, the Dirichlet condition specifies the function value along the boundary of the domain, the Neumann condition specifies the function's normal derivative value along the boundary, and the mixed condition specifies a Dirichlet condition on one portion of the boundary and a Neumann condition on the other. In presenting this boundary value problem, we are fundamentally interested in pre-

scribing a set of boundary conditions on the fluid variables which aptly represent the physical interaction between a laser and its surrounding fluid in a finite, 2D domain. This signals a departure from a purely abstracted treatment of the problem, as we must now consider how the 2D case may be derived from an inherently 3D phenomenon. We now consider several modalities by which to derive an appropriate set of boundary conditions from a physical arrangement of the laser in space.

2.1.2.1 Infinite Outer Boundary

One case of particular interest to both a physical and mathematical understanding of the steady-state is that of an inner domain Ω and an outer domain $U = \mathbb{R}^2 \backslash \Omega$ which tends toward infinity in all directions. That is, we consider the solution to the system (3) on all space $\mathbb{R}^2$ and attempt to extrapolate appropriate boundary conditions along the boundary of the inner domain $\partial\Omega$. We may consider this construction to be appropriate for determining the fluid dynamics in the region directly surrounding a laser where there is no physical boundary surrounding the fluid of a similar size to the domain Ω. A reasonable scenario where this is the case would be the propagation of a laser through the atmosphere or the propagation of a laser through a large room where we are only interested in the fluid dynamics directly surrounding the laser. This proposition of course assumes that we neglect any inherently turbulent properties of the fluid in reaching the steady-state dynamics. We will soon come to see that while this approach may seem reasonable, difficulties arise in the corresponding mathematical formulation due to the nature of the steady-state problem and the 2D structure of our domain. Let's begin by considering the domain $\Omega_B \subseteq \mathbb{R}^2$ where we seek to find a general solution to the Poisson equation of the form

$$\Delta u(\mathbf{x}) = f(\mathbf{x}), \quad \mathbf{x} \in \Omega_B \tag{8}$$

where there are no prescribed boundary conditions. One classical approach to solving this problem is to first find the solution G to the problem

$$\Delta G(\mathbf{x};\boldsymbol{\xi}) = \delta(\mathbf{x}-\boldsymbol{\xi}), \quad (\mathbf{x};\boldsymbol{\xi}) \in \Omega_B \tag{9}$$

where $\delta(\mathbf{x})$ is the Dirac delta distribution [17] such that

$$\iint_{\Omega_B} \delta(\mathbf{x}-\boldsymbol{\xi}) d\boldsymbol{\xi} = 1 \tag{10}$$

and

$$\iint_{\Omega_B} f(\boldsymbol{\xi})\delta(\mathbf{x}-\boldsymbol{\xi}) d\boldsymbol{\xi} = f(\mathbf{x}) \tag{11}$$

for some function $f(\mathbf{x})$ where $\mathbf{x} = (x, y)$ and $\boldsymbol{\xi} = (\xi, \eta)$. Such a solution G is called the fundamental solution to the Laplace equation or the free-space Green's function of the Laplace equation. This is a classical result in the study of the Poisson equation and it can be derived by applying the Divergence theorem and Green's theorem to an integration of the function G. An in depth derivation is provided in [17] and [18] where the final result becomes:

$$G(\mathbf{x};\boldsymbol{\xi}) = \frac{1}{2\pi} \log \sqrt{(x-\xi)^2 + (y-\eta)^2}. \tag{12}$$

Now by the property of the Dirac delta distribution defined by equation (11) and with G being a fundamental solution to the Poisson equation (9), we see that by the

linearity of the Laplace operator:

$$\begin{aligned}\Delta u(\mathbf{x}) &= f(\mathbf{x}) \\ &= \iint_{\Omega_B} f(\boldsymbol{\xi})\delta(\mathbf{x}-\boldsymbol{\xi})d\boldsymbol{\xi} \\ &= \iint_{\Omega_B} f(\boldsymbol{\xi})\Delta_{\mathbf{x}} G(\mathbf{x};\boldsymbol{\xi})d\boldsymbol{\xi} \\ &= \Delta \iint_{\Omega_B} f(\boldsymbol{\xi})G(\mathbf{x};\boldsymbol{\xi})d\boldsymbol{\xi}.\end{aligned} \tag{13}$$

Hence, we see that

$$\phi(\mathbf{x}) = \frac{1}{2\pi}\iint_{\Omega_B} f(\boldsymbol{\xi}) \log\sqrt{(x-\xi)^2+(y-\eta)^2}d\boldsymbol{\xi} \tag{14}$$

is a solution to the Poisson equation defined in (8). The null space of the Laplacian operator consists of the set of all harmonic functions $\psi(\mathbf{x})$ which satisfy $\Delta\psi = 0$, so we conclude that the general solution to (8) becomes

$$u(\mathbf{x}) = \phi(\mathbf{x}) + \psi(\mathbf{x}) \tag{15}$$

or any harmonic function ψ. We now recall that we seek to determine a suitable $u(\mathbf{x})$ which satisfies (8) such that we may determine appropriate boundary conditions for the steady-state fluid Poisson problem defined by equations (5)–(7). Since the free-space problem is determined only up to an arbitrary harmonic function, we can impose certain characteristics on the free space solution $u(\mathbf{x})$ to obtain a unique $\psi(\mathbf{x})$. By applying Green's second identity for the functions $H(\mathbf{x}), K(\mathbf{x}) \in C^2(\Omega_B)$ and an arc length element γ we obtain

$$\oint_{\partial\Omega_B}\left(H\frac{\partial K}{\partial \mathbf{n}} - K\frac{\partial H}{\partial \mathbf{n}}\right)d\gamma = \iint_{\Omega_B}(H\Delta K - K\Delta H)d\Omega_B. \tag{16}$$

It can then be shown [18] that the fundamental solution $G(\mathbf{x}, \boldsymbol{\xi})$ satisfies this identity, whereby substituting in $H = u(\mathbf{x})$ and $K = G(\mathbf{x}, \boldsymbol{\xi})$ we observe

$$\oint_{\partial\Omega_B} (u(\boldsymbol{\xi})\frac{\partial G(\mathbf{x};\boldsymbol{\xi})}{\partial \mathbf{n}} - G(\mathbf{x};\boldsymbol{\xi})\frac{\partial u(\boldsymbol{\xi})}{\partial \mathbf{n}})d\gamma = \iint_{\Omega_B} (u(\boldsymbol{\xi})\Delta G(\mathbf{x};\boldsymbol{\xi}) - G(\mathbf{x};\boldsymbol{\xi})\Delta u(\boldsymbol{\xi}))d\boldsymbol{\xi}. \tag{17}$$

recalling that G solves (9) and that we seek $u(\mathbf{x})$ such that $\Delta u(\mathbf{x}) = f(\mathbf{x})$, we obtain Green's third identity which takes the form

$$u(\mathbf{x}) = \iint_{\Omega_B} f(\boldsymbol{\xi})G(\mathbf{x};\boldsymbol{\xi})d\boldsymbol{\xi} + \oint_{\partial\Omega_B} u(\boldsymbol{\xi})\frac{\partial G(\mathbf{x};\boldsymbol{\xi})}{\partial \mathbf{n}} - G(\mathbf{x};\boldsymbol{\xi})\frac{\partial u(\boldsymbol{\xi})}{\partial \mathbf{n}}d\gamma = \phi(\mathbf{x}) + \psi(\mathbf{x}). \tag{18}$$

Equation (18) thus expresses the arbitrary harmonic function in terms of the solution itself and the fundamental solution to the free-space problem. We now seek to incorporate several characteristics of the solution $u(\mathbf{x})$ solved over the domain Ω_B. Since we're interested in determining boundary conditions for the local, steady-state fluid dynamics for a laser, it is reasonable to impose the condition that the free-space solution $u(\mathbf{x}) \to 0$ as $|\mathbf{x}| \to \infty$ asymptotically fast such that

$$\oint_{\partial\Omega_B} u(\boldsymbol{\xi})\frac{\partial G(\mathbf{x};\boldsymbol{\xi})}{\partial \mathbf{n}}d\gamma \to 0$$

as Ω_B grows large relative to the interior domain Ω. We would also expect the normal derivatives of each fluid variable to diminish as the domain size grows larger, so we impose a similar condition on the normal derivative $\frac{\partial u}{\partial \mathbf{n}}$ such that

$$\left| \oint_{\partial\Omega_B} G(\mathbf{x};\boldsymbol{\xi})\frac{\partial u(\boldsymbol{\xi})}{\partial \mathbf{n}}d\gamma \right| \leq M$$

for some constant $M \geq 0$. By Liouville's theorem, a classical result [19], we have that the harmonic function ψ is constant such that $\psi(\mathbf{x}) = M$ and it thus follows that the

free-space solution becomes

$$u(\mathbf{x}) = \frac{1}{2\pi} \iint_{\Omega_B} f(\boldsymbol{\xi}) \log \sqrt{(x-\xi)^2 + (y-\eta)^2} d\boldsymbol{\xi} + M. \tag{19}$$

We immediately see that by fixing (ξ, η), the absolute value of the integrand $|f(\boldsymbol{\xi}) \log \sqrt{(x-\xi)^2 + (y-\eta)^2}| \to \infty$ as $|\mathbf{x}| \to \infty$ for a function $f(\boldsymbol{\xi}) \neq 0$. Hence, if we fix the function $f(\boldsymbol{\xi}) > 0$ for all $\in \Omega_B$ and impose the condition that $f(\mathbf{x}) \to 0$ as $|\mathbf{x}| \to \infty$, then it is apparent that for the free-space solution, $|u(\mathbf{x})| \to \infty$ as $|\mathbf{x}| \to \infty$ so the vanishing boundary constraint imposed on $u(\mathbf{x})$ is invalid as the domain Ω_B approaches all of $\mathbb{R}^2$. We are now faced with a peculiarity in that the free space solution for the problem defined in (8) grows toward infinity as the domain Ω_B approaches $\mathbb{R}^2$ when the function $f(\mathbf{x})$ itself vanishes along the same boundary. This arises due to the nature of the fundamental solution $G(\mathbf{x}; \boldsymbol{\xi})$ to the free-space problem in that $G(\mathbf{x}; \boldsymbol{\xi}) \to \infty$ as $|\mathbf{x}| \to \infty$ for a fixed $\boldsymbol{\xi}$ and vice versa. Therefore, when attempting to construct a free-space solution to the Poisson problem, this property precludes a free-space solution which vanishes as the domain grows larger. This difficulty exists only for the 2D problem, wherein for higher dimensions the fundamental solution tends to vanish at the boundary. When we consider the steady-state a real fluid in 2D, these findings suggest that, paradoxically, fluid variables like velocity, temperature, and pressure will continue to grow as their domain of consideration increases to encompass all space. Obviously, this is an impossible scenario which follows from basic cosmological and thermodynamic properties of the universe [20]. The only resolution for the 2D problem, then, is to impose boundary conditions along the inner domain Ω which represent either a physical barrier or conditions by which a steady-state can be locally achieved. The following sections will thus identity several of these approaches where we hereafter abandon the free-space approach in the 2D problem.

2.1.2.2 Finite Boundaries

An alternative approach to developing boundary conditions of the form (5)–(7) for each fluid variable is to consider such conditions which may be systematically implemented in an experimental setup of a laser propagating through a finite box. Research involving the fluid dynamics surrounding finite geometries is ubiquitous [21]. We will first consider a closed-box approach for the domain Ω where we impose the condition that no fluid may penetrate the boundary $\partial\Omega$. From this initial assumption, two of the most common boundary conditions imposed on flows in finite geometries are the no-slip condition and the slip condition. The no-slip condition is commonly imposed on fluids which travel in a single direction along a boundary wall and states that both the normal and tangential velocity components along the boundary are stationary. Since the laser forcing radiates symmetrically outward from the center of the domain, we expect circular fluid movement and we thus reject a no-slip condition since it precludes any fluid velocity along the boundary. The slip condition, conversely, allows for non-zero tangential fluid velocity along the boundary where it requires the normal derivative of the tangential velocity to be zero. Since there is no fluid velocity going into the boundary, we also specify that the pressure and subsequently the temperature along the boundary are equal to zero. If we suppose that the boundary consists of the disjoint union $\partial\Omega = \partial\Omega_{\text{top}} \cup \partial\Omega_{\text{bottom}} \cup \partial\Omega_{\text{left}} \cup \partial\Omega_{\text{right}}$ then these conditions can be equivalently stated as

$$v(x,y) = 0, \quad \frac{\partial u(x,y)}{\partial \mathbf{n}} = 0, \quad (x,y) \in \partial\Omega_{\text{top}} \cup \partial\Omega_{\text{bottom}}, \tag{20a}$$

$$u(x,y) = 0, \quad \frac{\partial v(x,y)}{\partial \mathbf{n}} = 0, \quad (x,y) \in \partial\Omega_{\text{left}} \cup \partial\Omega_{\text{right}}, \tag{20b}$$

$$T(x,y) = 0, \quad (x,y) \in \partial\Omega, \tag{20c}$$

$$P(x,y) = 0, \quad (x,y) \in \partial\Omega. \tag{20d}$$

With respect to the Poisson boundary value problems defined in equations (5)-(7), this boundary condition represents a Dirichlet type on the fluid temperature and pressure and a mixed type on the fluid velocity components. A common modification of the slip condition is to impose a zero pressure gradient along the boundary such that the pressure boundary value problem becomes a Neumann type. These slip conditions work well for the case of closed-box in 2D, and we will see in Chapter IV that steady solutions do exist for certain Re, Ri, Pe numbers and laser forcing amplitudes. We also note that due to the 2D construction of the problem, we cannot account for 3D effects arising from the domain boundaries in the direction of the propagating laser. In Chapter V, we will discuss several pertinent issues associated with the limitations of a 2D problem.

If we instead choose to allow the fluid to escape out of the top and bottom of the domain $\partial\Omega$, then the slip condition no longer applies. By allowing this freedom of movement, we may obtain a steady-state solution which more accurately represents the fluid dynamics in open space. Coupled with this boundary flexibility, however, is the burden of providing *a priori* boundary conditions for each fluid variable along the free-flowing boundaries. Determining such boundary conditions is a difficult task and requires an experimental approach to developing the appropriate boundary profiles of the fluid variables. For example, we may specify a temperature, pressure, and velocity profile along the top and bottom boundaries while insulating the sides such that the normal derivative of temperature is zero. Any attempt at establishing boundary conditions of this kind must be informed by the possibilities of an experimental setup in controlling the fluid variables along the boundary. The focus of this research is on the development of methodologies to determine solutions to the steady-state Navier–Stokes equations, and as such, we suspend an in depth treatment of experimental for future research in the field. One example solution utilizing experimental boundary

conditions, however, is presented in Chapter IV. The final and most involved set of boundary conditions we discuss is the open boundary condition approach. An open boundary condition is similar to the infinite outer boundary discussed earlier in that it imposes no conditions on the solution along the boundary of the inner domain Ω by allowing the solution to exist outside of Ω. Fornberg [22] has developed and Morrill [15] has implemented an open boundary condition for laser propagation in 2D wherein an interior and exterior domain is established and such that the stream function evaluated along exterior domain is a linear transformation of the stream function of the exterior domain. This approach is optimal for accurately predicting solutions with a free flowing boundary, yet is undesirable with respect to its complexity. Chapter V includes a discussion on how an open boundary condition of this type could be imposed and how it compares to the other boundary conditions discussed above.

2.2 Numerical Algorithms and Analysis

We now recall one of the fundamental purposes of our study: we seek to develop a novel methodology by which to solve the system of equations (4) with the classical Dirichlet, Neumann, and mixed boundary conditions over the domain Ω. Since this is a coupled, nonlinear system of partial differential equations, there is no generalized approach to solving the equations analytically. Instead, we proceed by utilizing a universally applied approach to solving the Navier-Stokes equations. That is, we develop a numerical algorithm which approximates the true solution to a sufficient degree of accuracy over a discrete grid. In Chapter I, we discussed various numerical approaches used in contemporary applied mathematics by which to solve different forms of the Navier-Stokes equations. Many beget their practicality in their ability to account for flows around complex geometries. In the steady-state laser-fluid interaction problem, however, there is a need for numerical solvers which are designed with

an emphasis on speed of convergence rather than versatility of domain discretization. It is precisely our ambition then to devise a numerical algorithm which is faster than canonical numerical methods available today. In Chapter III, we describe in detail this numerical algorithm through which we discretize and solve the system (4). In this section, therefore, we introduce the relevant background in numerical analysis required to develop our numerical algorithm and to compare it to a more common Newton method approach.

2.2.1 Poisson Equation Solvers

The precise numerical method we introduce in Chapter III to solve the equations (4) with classical boundary conditions requires a numerical approach to solving successive Poisson equations of the form (5)–(7) where the function f_j is completely determined at each grid point in the discretization of the domain Ω. Based on this numerical schema, we introduce below the applicable procedures and results by which to numerically solve a Poisson boundary value problem over a 2D grid.

Recall the rectangular domain $\Omega = [-0.5, 0.5] \times [-0.5, 0.5]$ defined in Figure 2. Let the discretized version of the domain be Ω_D where we discretize Ω by spacing grid points of width h in the x direction and width k in the y direction. Figure 3 provides a diagram for how the domain discretized into a rectangular grid where each grid point is enumerated moving horizontally.

For the remainder of this study, we assume a uniform, square grid with even spacing such that $h = k$. The goal of the discrete Poisson solver is to find a matrix $\mathbf{A}$ such that at each grid point P_q, the solution $\mathbf{u_D}$ to the matrix equation

$$\mathbf{A}\mathbf{u_D} = \mathbf{f} \tag{21}$$

is an accurate estimate of the solution to the Poisson equation $\Delta u = f$ for some clas-

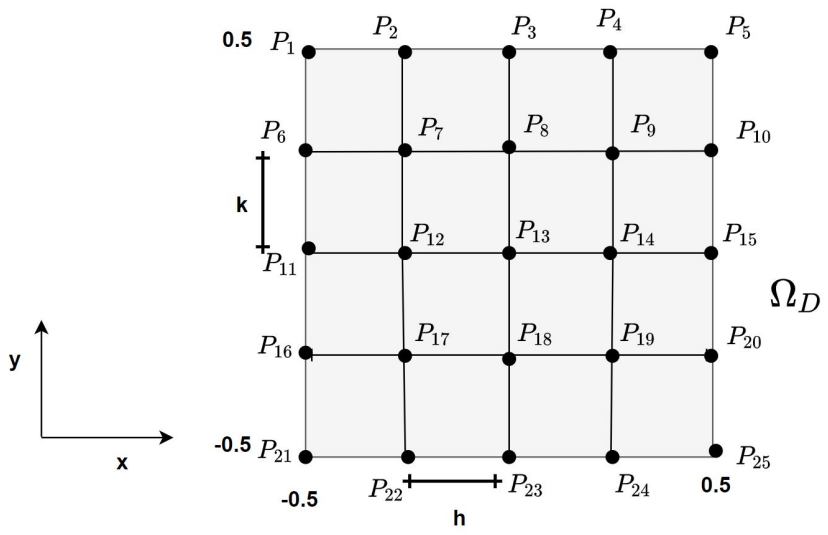

Figure 3: Discretized domain Ω_D showing the enumeration of the grid points P_q with $h = k = 1/4$.

sical boundary condition. This procedure requires discretizing the Laplace operator and accounting for the boundary conditions at each point along the grid. Therefore, we utilize finite difference methods to estimate the second derivatives in the Laplacian $\Delta = u_{xx} + u_{yy}$. For grid indices i, j, the centered-difference formula for the second derivatives yields

$$\left(\frac{\partial^2 u}{\partial x^2}\right)_{ij} = \frac{u_{i+1,j} - 2u_{ij} + u_{i-1,j}}{h^2} + \mathcal{O}(h^2), \tag{22a}$$

$$\left(\frac{\partial^2 u}{\partial y^2}\right)_{ij} = \frac{u_{i,j+1} - 2u_{ij} + u_{i,j-1}}{h^2} + \mathcal{O}(h^2) \tag{22b}$$

so the pointwise discrete Laplacian becomes

$$(\Delta u)_{ij} = \frac{u_{i+1,j} + u_{i-1,j} - 4u_{i,j} + u_{i,j+1} + u_{i,j-1}}{h^2} + \mathcal{O}(h^2). \tag{23}$$

This discretization is commonly referred to as a five-point stencil, where at each interior grid point the representation of the equation $\Delta u_{ij} = h f_{ij}$ is given diagrammatically in Figure 4.

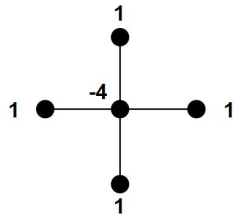

$$\begin{pmatrix} & 1 & \\ 1 & -4 & 1 \\ & 1 & \end{pmatrix}$$

Figure 4: Five-point stencil for discrete Laplacian at each grid point.

With an established schema for discretizing the second derivatives, we now focus on implementation of the boundary conditions within the numerical algorithm.

2.2.1.1 Dirichlet Boundary Conditions

Suppose that we seek to find a numerical solution to the Dirichlet problem

$$\begin{cases} \Delta u_{ij} = f_{ij}, & (x_i, y_i) \in \Omega_D, \\ u_{ij} = g_{ij}, & (x_i, y_i) \in \partial\Omega_D. \end{cases} \tag{24}$$

Since the boundary points are completely determined by the function g_{ij}, we need only to solve for the interior grid points. This is accomplished by applying the five-point stencil for the Laplacian at each interior point $(x_i, y_j) \in \Omega_D \setminus \partial\Omega_D$ such that we obtain a system of equations defined by

$$u_{i+1,j} + u_{i-1,j} - 4u_{i,j} + u_{i,j+1} + u_{i,j-1} = h^2 f_{ij} \tag{25}$$

and the boundary points are assigned the value $u_{ij} = g_{ij}$ for $(x_i, y_j) \in \partial\Omega_D$. To maintain a symmetric positive-definite matrix $\tilde{\mathbf{A}}$, one may solve only for the interior points in the matrix equation $\tilde{\mathbf{A}}\mathbf{u}_I = h\tilde{\mathbf{f}}_I$ where $\tilde{\mathbf{f}}_I$ accounts for the values of the boundary points in the stencil when needed. An alternative formulation is to devise the matrix $\mathbf{A}$ such that the boundary value assignments occur implicitly in the matrix

equation $\mathbf{A}\mathbf{u}_D = h^2\hat{\mathbf{f}}$ where $a_{ii} = 1$ and $f_{ij} = \frac{1}{h^2}g_{ij}$ for $(x_i, y_j) \in \partial\Omega_D$. This allows one to solve for each grid point at the same time, but increases the size of the matrix. Either approach can be easily implemented in a suitable programming language in which a multitude of algorithms exist for solving linear systems of equations.

2.2.1.2 Neumann Boundary Conditions

We now suppose that we seek to find a numerical solution to the Neumann boundary value problem

$$\begin{cases} \Delta u_{ij} = f_{ij}, & (x_i, y_i) \in \Omega_D, \\ \left(\frac{\partial u}{\partial \mathbf{n}}\right)_{ij} = w_{ij}, & (x_i, y_i) \in \partial\Omega_D. \end{cases} \tag{26}$$

A compatibility condition exists between the function f and the function w which specifies the normal derivative along the boundary. Recall that the divergence theorem for compact domains $\Omega \subset \mathbb{R}^2$ and continuously differentiable vector fields $\mathbf{F}$ states that

$$\iint_\Omega (\nabla \cdot \mathbf{F})\, dA = \oint_{\partial\Omega} \mathbf{F} \cdot \hat{\mathbf{n}} d\gamma, \tag{27}$$

so by allowing $\mathbf{F} = \nabla u$ such that $\nabla \cdot \mathbf{F} = \nabla \cdot \nabla u = \Delta u$, we obtain the compatibility condition for the Neumann problem

$$\iint_\Omega f dA = \iint_\Omega \Delta u dA = \oint_{\partial\Omega} \frac{\partial u}{\partial \mathbf{n}} d\gamma = \oint_{\partial\Omega} w d\gamma, \tag{28}$$

where the area integral of f over Ω must be equal to the contour integral of h over $\partial\Omega$ for a solution to the Neumann problem to exist. In addition to this complication, the discretization of the Neumann problem introduces difficulty in that the normal derivatives of u along the boundary must be approximated using a finite difference scheme. To maintain the same order of accuracy for the first and second derivatives,

we employ the centered difference scheme for first-order derivatives

$$\left(\frac{\partial u}{\partial x}\right)_{ij} = \frac{u_{i+1,j} - u_{i-1,j}}{2h} + \mathcal{O}(h^2), \tag{29a}$$

$$\left(\frac{\partial u}{\partial y}\right)_{ij} = \frac{u_{i,j+1} - u_{i,j-1}}{2h} + \mathcal{O}(h^2). \tag{29b}$$

Along the boundary, only of of these points will exist within the grid. To rectify the situation, we employ the ubiquitous ghost point method described by Chen [23] where we temporarily extend the grid to allow points alongside each boundary to exist. If we consider the left boundary at $x = -0.5$ such that the index $i = 1$, then by applying the discrete versions of the Poisson equation (26a) and the boundary condition (26b), we obtain the system of equations

$$-4u_{1,j} + u_{0,j} + u_{2,j} + u_{1,j-1} + u_{1,j+1} = h^2 f_{1,j}, \tag{30a}$$

$$u_{0,j} - u_{2,j} = 2hw_{1,j}, \tag{30b}$$

where by the second equation we can solve for the ghost point $u_{0,j} = 2hw_{1,j} + u_{2,j}$ and substitute in to obtain the single equation for points along the boundary

$$-4u_{1,j} + 2u_{2,j} + u_{1,j-1} + u_{1,j+1} = h^2 f_{1,j} - 2hw_{1,j}. \tag{31}$$

For each non-corner boundary point, the same procedure applies. For the corner points, however, the normal derivative is undefined. To deal with this issue, we take the normal derivative to be the average of the derivatives in the x and y direction, where by utilizing the same approach given in equations (30) and solving for the associated ghost points, we obtain the discrete equation at the corner points to be

(for the case of $i = j = 1$)

$$-4u_{1,1} + 2u_{2,1} + 2u_{1,2} = h^2 f_{1,1} - 4hw_{1,1}. \tag{32}$$

With each grid point thus endowed with a linear equation, we may solve a system of the form $\mathbf{A}\mathbf{u}_D = \mathbf{f}$ where the matrix $\mathbf{A}$ is banded. One can show that $\mathbf{A}$ is symmetric semi-definite with a null space consisting of all vectors which are equal to a constant vector. As such, to obtain a unique solution, Chen [23] shows that a discrete version of the compatibility condition 28 takes the form

$$\sum_q \mathbf{f}_\mathbf{q} = 0, \tag{33}$$

where we can assign $\tilde{\mathbf{f}} = \mathbf{f} - \overline{\mathbf{f}}$ with $\overline{\mathbf{f}}$ being the mean of $\mathbf{f}$ to satisfy this condition.

2.2.1.3 Mixed Boundary Conditions

If we instead consider the numerical solution to the mixed boundary value problem

$$\begin{cases} \Delta u_{ij} = f_{ij}, & (x_i, y_i) \in \Omega_D, \\ u_{ij} = g_{ij}, & (x_i, y_i) \in \partial\Omega_{D,D}, \\ \left(\frac{\partial u}{\partial \mathbf{n}}\right)_{ij} = w_{ij}, & (x_i, y_i) \in \partial\Omega_{D,N}, \end{cases} \tag{34}$$

we must employ a combination of the techniques used in the Dirichlet and Neumann cases. If we partition each boundary point into a Dirichlet boundary $\partial\Omega_{D,D}$ or a Neumann boundary $\partial\Omega_{N,D}$, then we may assign a linear equation to each respective grid point based on their classification. For example, if we consider a slip boundary condition for the x-direction fluid velocity $u(x, y)$, then the top and bottom boundaries becomes a Neumann type and the side boundaries become a Dirichlet type which

include the corner points. Since each grid point produces a linear equation, the mixed boundary value problem can be solved discretely in the form $\mathbf{A}\mathbf{u}_D = \mathbf{f}$ where $\mathbf{u}_D$ is unique due to the explicit assignments of the Dirichlet grid points.

2.2.2 Newton Solver

One classical approach commonly applied to solving nonlinear systems of algebraic equations is Newton's method. Newton's method is an iterative, fixed-point scheme which seeks to find the roots of continuously differentiable functions. That is, for a real, vector-valued function $\mathbf{F} : \mathbb{R}^m \to \mathbb{R}^m$ with input $\mathbf{x}$, Newton's method proceeds to iteratively calculate the roots $\mathbf{x}^*$ such that $\mathbf{F}(\mathbf{x}^*) = \mathbf{0}$. This is accomplished through the iteration

$$\mathbf{x}_{k+1} = \mathbf{x}_k - \mathbf{J}^{-1}\mathbf{F}(\mathbf{x}_k) \tag{35}$$

where $\mathbf{J}$ is the Jacobian matrix of $\mathbf{F}$ and $\mathbf{x}_0$ is some *a priori* guess on the solution which falls into a region such that the iteration converges. Since Newton's method only applies to systems of algebraic equations, we must apply some algebraic approximation to the derivatives of a system of pdes of the form (4). This is accomplished through a discretization of the domain Ω and by applying finite difference formulas to each of the derivative terms in a system of pdes. It is a well-established result in numerical analysis that Newton's method converges at least linearly with most problems converging quadratically. That is, the error between the current iteration $\mathbf{x}_k$ and the root $\mathbf{x}^*$ is bounded by the error between the previous iteration and the root such that

$$\|\mathbf{x}_k - \mathbf{x}^*\|_p \leq C\|\mathbf{x}_{k-1} - \mathbf{x}^*\|_p^2 \tag{36}$$

for some constant C and a vector p-norm. Based on the simplicity of the approach and the fast rate of convergence, this approach is immensely useful. The major

downside, however, is that it can become massively computationally expensive as the discretized domain becomes more refined. Accordingly, we will compare the computational expense and convergence regions between Newton's method and the novel numerical approach described in the following chapter.

III. Methodology

This chapter serves as an explication of the methodological approach in which we develop a convergent numerical algorithm for finding stead-state solutions to the Navier–Stokes equations. We employ the mathematical theory introduced in the previous section to perform a convergence analysis and to describe the process of the implementation of the numerical algorithm. Various potential approaches are discussed, wherein the chosen techniques are justified with respect to their desired numerical properties. This convergence analysis, coupled with the numerical method, will then allow for a careful treatment of physical results in Chapter IV which provide informative insights into the physical nature of laser-fluid interaction.

3.1 Convergence Analysis

Recall that we seek to solve for fluid velocity, pressure, and temperature in the buoyancy-driven, Boussinseq fluid approximation for the Navier–Stokes equations over some finite rectangular domain Ω. In this analysis, we assume small laser forcing such that each fluid variable may be represented as a perturbation from a resting fluid steady-state. One of the assumptions imposed on this problem as described in section 2.1 is that the laser forcing can be modeled as a function of (x, y) over the domain Ω. We assume that the laser irradiance takes on a Gaussian profile of the form

$$F(x, y) = \varepsilon e^{-c(x^2+y^2)} = \varepsilon f(x, y), \tag{37}$$

where ε is a constant representing the max laser amplitude and c is a constant accounting for the decay rate of the forcing about the origin. We now define $\hat{u}$, $\hat{v}$, $\hat{T}$, and $\hat{p}$ as the exact horizontal velocity, vertical velocity, temperature, and pressure, respectively. We restate equation (4) for the steady Navier–Stokes equations in the

Boussinseq approximation as

$$\begin{aligned}
\Delta\hat{u} &= Re\left((\hat{\mathbf{u}}\cdot\nabla)\hat{u} - \hat{p}_x\right), && \text{(38a)}\\
\Delta\hat{v} &= Re\left((\hat{\mathbf{u}}\cdot\nabla)\hat{v} - \hat{p}_y - Ri\hat{T}\right), && \text{(38b)}\\
\Delta\hat{p} &= \nabla\cdot(\hat{\mathbf{u}}\cdot\nabla)\hat{\mathbf{u}} - Ri\hat{T}_y, && \text{(38c)}\\
\Delta\hat{T} &= Pe\left((\hat{\mathbf{u}}\cdot\nabla)\hat{T} - F\right). && \text{(38d)}
\end{aligned}$$

Due to the accessibility and desirable properties of discrete Poisson solvers, we are now motivated to devise a convergent iterative scheme which makes use of successive Poisson solves on the fluid variables. We define this iteration for $n > 1$ by

$$\begin{aligned}
\Delta\hat{u}_n &= Re\left((\hat{\mathbf{u}}_{n-1}\cdot\nabla)\hat{u}_{n-1} - \frac{\partial\hat{p}_n}{\partial x}\right), && \text{(39a)}\\
\Delta\hat{v}_n &= Re\left((\hat{\mathbf{u}}_{n-1}\cdot\nabla)\hat{v}_{n-1} - \frac{\partial\hat{p}_n}{\partial y} - Ri\hat{T}_n\right), && \text{(39b)}\\
\Delta\hat{p}_n &= \nabla\cdot(\hat{\mathbf{u}}_{n-1}\cdot\nabla)\hat{\mathbf{u}}_{n-1} - Ri\frac{\partial\hat{T}_n}{\partial y}, && \text{(39c)}\\
\Delta\hat{T}_n &= Pe\left((\hat{\mathbf{u}}_{n-1}\cdot\nabla)\hat{T}_{n-1} - \varepsilon f\right), && \text{(39d)}
\end{aligned}$$

where we initialize the solution as

$$\begin{aligned}
\Delta\hat{u}_0 &= -Re\frac{\partial\hat{p}_0}{\partial x}, && \text{(40a)}\\
\Delta\hat{v}_0 &= -Re\left(\frac{\partial\hat{p}_0}{\partial y} + Ri\hat{T}_0\right), && \text{(40b)}\\
\Delta\hat{p}_0 &= -Ri\frac{\partial\hat{T}_0}{\partial y}, && \text{(40c)}\\
\Delta\hat{T}_0 &= -Pe(\varepsilon f). && \text{(40d)}
\end{aligned}$$

This initialization is the linearization of the system of equations and thus should serve as a strong initial guess for small amplitude solutions. We now state a crucial theorem

which motivates our study of convergence:

Theorem 1 (**Banach Fixed-Point Theorem (Contraction Mapping Theorem)).** *Let (X, d) be a complete metric space and let $f : X \to X$ be a contraction. Then there is one and only one point x_0 in X such that*

$$f(x_0) = x_0.$$

Moreover, if x is any point in X and x_n is defined inductively by $x_1 = f(x)$, $x_2 = f(x_1)$, ..., $f(x_n) = f(x_{n-1})$, then $x_n \to x_0$ as $n \to \infty$.

Proof. Classic result. Theorem and proof can be seen in Naylor and Sell [24]. □

We will next show that this iteration converges for small ε. The iteration was constructed so that its fixed points are steady solutions of (38), so this convergence of the scheme gives existence of solutions. We state this result as a theorem:

Theorem 2 (**Convergence of Steady Solutions to the Boussinesq Navier-Stokes equations).** *The iteration defined in (39) and (40) converges to unique solutions for small forcing and Dirichlet boundary conditions.*

Proof. We begin by stating a definition from Brezis [25] and two lemmas which assist in our analysis:

Definition 1 (**Sobolev Spaces**). *Let $\Omega \subset \mathbb{R}^N$ and let $p \in \mathbb{R}$ with $1 \leq p \leq \infty$. If $m \geq 2$ is an integer, then the Sobolev space $W^{m,p}(\Omega)$ is defined for all α with $|\alpha| \leq m$,*

$$W^{m,p}(\Omega) = \{u \in L^p(\Omega) : \exists g_\alpha \in L^p(\Omega) \text{ s.t. } \int_\Omega u D^\alpha \varphi = (-1)^{|\alpha|} \int_\Omega g_\alpha \varphi \quad \forall \varphi \in C_c^\infty(\Omega)\}, \tag{41}$$

where we employ the multi-index notation $\alpha = (\alpha_1, \alpha_2, ..., \alpha_N)$ *such that*

$$|\alpha| = \sum_{i=1}^{N} \alpha_i, \qquad D^\alpha \varphi = \frac{\partial^{|\alpha|}\varphi}{\partial x_1^{\alpha_1} \partial x_2^{\alpha_2} ... \partial x_N^{\alpha_N}}. \tag{42}$$

We assign the $g_\alpha = D^\alpha u$*. The space* $W^{m,p}(\Omega)$ *equipped with the norm*

$$\|u\|_{W^{m,p}} = \sum_{|\alpha| \leq m} \|D^\alpha u\|_{L^p} \tag{43}$$

is a Banach space and we define the space

$$H^m(\Omega) = W^{m,2}(\Omega). \tag{44}$$

Lemma 1 (H^s **is an algebra).** *Let* $\Omega \subset \mathbb{R}^d$*. Suppose* $s_1, s_2 \geq s$ *and* $s_1 + s_2 > s + d/2$*. Then* $u \in H^{s_1}(\Omega)$ *and* $v \in H^{s_2}(\Omega)$ *gives that* $(uv) \in H^s(\Omega)$*, and that*

$$\|uv\|_{H^s} \leq M \|u\|_{H^{s_1}} \|v\|_{H^{s_2}}$$

where M *depends only on* s_1, s_2 *and* d*.*

Proof. Standard result. See [26] for proof. □

Lemma 2 (**Elliptic Estimate).** *If* $F \in L^p(\Omega)$ *such that* $\|F\|_{L^p(\Omega)} < \infty$ *then there exists a unique solution to*

$$\Delta u = F \qquad x \in \Omega = [a, b] \times [c, d]$$

with

$$u|_{\partial\Omega} = 0,$$

And that solution satisfies $\|u\|_{W^{2,p}(\Omega)} \leq C \|F\|_{L^p(\Omega)}$ *where* $C = C(a, b, c, d, p)$ *is a*

positive constant.

Proof. Standard result, see [27] for proof. A similar result also exists for inhomogeneous and Neumann boundary conditions for boundary data which satisfy compatibility conditions as described in [28] and [29]. □

We now introduce the small amplitude assumption on the dynamics, where each $\hat{u}, \hat{v}, \hat{p}, \hat{T}$ is represented by a perturbation from the resting fluid case:

$$\hat{u} = \varepsilon u, \tag{45a}$$

$$\hat{v} = \varepsilon v, \tag{45b}$$

$$\hat{p} = \varepsilon p, \tag{45c}$$

$$\hat{T} = \varepsilon T. \tag{45d}$$

The main work of the proof is to construct the equation for the difference between u_n and u_m (and similarly v_n and v_m, p_n and p_m, T_n and T_m) by applying the representation in (45) and subtracting (39) at these two indices:

$$\begin{aligned}&\Delta(\mathbf{u}_n - \mathbf{u}_m)\\ &= Re(\varepsilon(\mathbf{u}_{n-1}\cdot\nabla)\mathbf{u}_{n-1} - \varepsilon(\mathbf{u}_{m-1}\cdot\nabla)\mathbf{u}_{m-1} - \nabla(p_n - p_m) - Ri(T_n - T_m)\mathbf{e_2}),\end{aligned} \tag{46a}$$

$$\begin{aligned}&\Delta(p_n - p_m)\\ &= \nabla\cdot(\varepsilon(\mathbf{u}_{n-1}\cdot\nabla)\mathbf{u}_{n-1} - \varepsilon(\mathbf{u}_{m-1}\cdot\nabla)\mathbf{u}_{m-1} - Ri(T_n - T_m)\mathbf{e_2}),\end{aligned} \tag{46b}$$

$$\begin{aligned}&\Delta(T_n - T_m)\\ &= \varepsilon Pe((\mathbf{u}_{n-1}\cdot\nabla)T_{n-1} - (\mathbf{u}_{m-1}\cdot\nabla)T_{m-1}).\end{aligned} \tag{46c}$$

We proceed by investigating the form of equation (46c) first. Define

$$F_T(n,m) = \varepsilon Pe((\mathbf{u}_{n-1}\cdot\nabla)T_{n-1} - (\mathbf{u}_{m-1}\cdot\nabla)T_{m-1}) \tag{47}$$

where we expand out the gradient operators and manipulate the form of the equation such that:

$$\begin{aligned} F_T(n,m) &= \varepsilon Pe((\mathbf{u}_{n-1}\cdot\nabla)T_{n-1} - (\mathbf{u}_{m-1}\cdot\nabla)T_{m-1}) \\ &= Pe\left(u_{n-1}\frac{\partial T_{n-1}}{\partial x} + v_{n-1}\frac{\partial T_{n-1}}{\partial x} - u_{m-1}\frac{\partial T_{m-1}}{\partial x} - v_{m-1}\frac{\partial T_{m-1}}{\partial x}\right) \\ &= \frac{\varepsilon Pe}{2}\left[(u_{n-1}-u_{m-1})\left(\frac{\partial T_{n-1}}{\partial x} + \frac{\partial T_{m-1}}{\partial x}\right) + (u_{n-1}+u_{m-1})\left(\frac{\partial T_{n-1}}{\partial x} - \frac{\partial T_{m-1}}{\partial x}\right)\right. \\ &\left. + (v_{n-1}-v_{m-1})\left(\frac{\partial T_{n-1}}{\partial y} + \frac{\partial T_{m-1}}{\partial y}\right) + (v_{n-1}+v_{m-1})\left(\frac{\partial T_{n-1}}{\partial y} - \frac{\partial T_{m-1}}{\partial y}\right)\right]. \end{aligned} \tag{48}$$

We now prove that the function $F_T(n,m) \in L^2(\Omega)$ such that the norm $\|F_T\|_{L^2(\Omega)} < \infty$ by showing that each $T_n, p_n, u_n, v_n \in H^2(\Omega)$ for $n, m \geq 0$.

Lemma 3 (**Sobolev Inclusion**). *If the normalized laser forcing $f(x,y) \in L^2(\Omega)$, then for $n, m \geq 0$, each $T_n, p_n, u_n, v_n \in H^2(\Omega)$ and $F_T(n,m) \in L^2(\Omega)$.*

Proof. Suppose that $f(x,y) \in L^2(\Omega)$. By recalling the initialization (40), we apply Lemma 2 to see that $T_0 \in H^2(\Omega)$. By the definition of the Sobolev space (41), it follows that $D^1 T_0 \in L^2(\Omega)$ and thus by applying Lemma 2 again it follows that $P_0 \in H^2(\Omega)$. A similar argument holds for u_0 and v_0. We now hypothesize for induction that each $T_n, p_n, u_n, v_n \in H^2(\Omega)$. The base case was just shown. Based on the iteration (39) and by applying the small amplitude assumption (45), we see that

$$\Delta T_{n+1} = Pe\left(\varepsilon(\mathbf{u}_n\cdot\nabla)T_n - f\right).$$

Since u_n and $T_n \in H^2(\Omega)$, we apply Lemma 1 with $s = s_1 = 0$ on the T_n derivatives and $s_2 = 2$ on the u_n, v_n functions to see that the right hand side is an $L^2(\Omega)$ function such that $T_{n+1} \in H^2(\Omega)$. A similar argument holds for each $p_{n+1}, u_{n+1}, v_{n+1}$ so we conclude that $T_n, p_n, u_n, v_n \in H^2(\Omega)$. Based on this Sobolev inclusion, we

may again apply Lemma 1 to the terms in the expression for $F_T(n,m)$ to see that $F_T(n,m) \in L^2(\Omega)$. $\square$

We now apply the triangle inequality to the norm of the expression (48) which yields,

$$\begin{aligned}\|F_T\|_{L^2(\Omega)} \leq \frac{\varepsilon Pe}{2} \Bigg[&\|(u_{n-1}-u_{m-1})\left(\frac{\partial T_{n-1}}{\partial x}+\frac{\partial T_{m-1}}{\partial x}\right)\|_{L^2} \\ &+ \|(u_{n-1}+u_{m-1})\left(\frac{\partial T_{n-1}}{\partial x}-\frac{\partial T_{m-1}}{\partial x}\right)\|_{L^2} \\ &+ \|(v_{n-1}-v_{m-1})\left(\frac{\partial T_{n-1}}{\partial y}+\frac{\partial T_{m-1}}{\partial y}\right)\|_{L^2} \\ &+ \|(v_{n-1}+v_{m-1})\left(\frac{\partial T_{n-1}}{\partial y}-\frac{\partial T_{m-1}}{\partial y})\right)\|_{L^2}\Bigg].\end{aligned} \tag{49}$$

Recall that we can define the Sobolev space

$$H^2(\Omega) = \{f \in L^2(\Omega) : D^\alpha f \in L^2(\Omega) \forall |\alpha| \leq 2\}.$$

The norm for $f \in H^2(\Omega)$ is then

$$\|f\|_{H^2(\Omega)} = \sum_{|\alpha|\leq 2} \|D^\alpha f\|_{L^2(\Omega)}.$$

By this definition, it then follows that

$$\frac{\partial T_{n-1}}{\partial x}, \frac{\partial T_{m-1}}{\partial x}, \frac{\partial T_{n-1}}{\partial y}, \frac{\partial T_{m-1}}{\partial y} \in L^2(\Omega).$$

Hence, by applying Lemma 1 with $s = s_1 = 0$ and $s_2 = 2$, we can establish the following inequalities on the norms:

$$\|(u_{n-1}-u_{m-1})\left(\frac{\partial T_{n-1}}{\partial x}+\frac{\partial T_{m-1}}{\partial x}\right)\|_{L^2(\Omega)} \leq M_T \|(u_{n-1}-u_{m-1})\|_{H^2(\Omega)} \|\frac{\partial T_{n-1}}{\partial x}+\frac{\partial T_{m-1}}{\partial x}\|_{L^2(\Omega)},$$

$$\|(u_{n-1}+u_{m-1})\left(\frac{\partial T_{n-1}}{\partial x}-\frac{\partial T_{m-1}}{\partial x}\right)\|_{L^2(\Omega)} \leq M_T\|(u_{n-1}+u_{m-1})\|_{H^2(\Omega)}\|\frac{\partial T_{n-1}}{\partial x}-\frac{\partial T_{m-1}}{\partial x}\|_{L^2(\Omega)},$$

$$\|(v_{n-1}-v_{m-1})\left(\frac{\partial T_{n-1}}{\partial y}+\frac{\partial T_{m-1}}{\partial y}\right)\|_{L^2(\Omega)} \leq M_T\|(v_{n-1}-v_{m-1})\|_{H^2(\Omega)}\|\frac{\partial T_{n-1}}{\partial y}+\frac{\partial T_{m-1}}{\partial y}\|_{L^2(\Omega)},$$

$$\|(v_{n-1}+v_{m-1})\left(\frac{\partial T_{n-1}}{\partial y}-\frac{\partial T_{m-1}}{\partial y}\right)\|_{L^2(\Omega)} \leq M_T\|(v_{n-1}+v_{m-1})\|_{H^2(\Omega)}\|\frac{\partial T_{n-1}}{\partial y}-\frac{\partial T_{m-1}}{\partial y}\|_{L^2(\Omega)}.$$

Note that by definition of the norm (43) in the Sobolev space $H^2(\Omega)$ for some $u \in H^2(\Omega)$, we can establish the inequality

$$\|\frac{\partial u}{\partial x}\|_{L^2(\Omega)}, \|\frac{\partial u}{\partial y}\|_{L^2(\Omega)} \leq \|u\|_{H^2(\Omega)}.$$

Finally, by applying Lemma 2 to the equation $(46c)$, we see that for $\|F_T(n,m)\|_{L^2(\Omega)} < \infty$, $T_n - T_m \in H_0^2(\Omega)$ with $\|T_n - T_m\|_{H^2(\Omega)} \leq C\|F_T\|_{L^2(\Omega)}$. We now establish the inequality on $\|T_n - T_m\|_{H^2(\Omega)}$ by:

$$\begin{aligned}\|T_n - T_m\|_{H^2(\Omega)} \leq \frac{\varepsilon PeCM_T}{2}\big(&\|(u_{n-1}-u_{m-1})\|_{H^2(\Omega)}\|(T_{n-1}+T_{m-1})\|_{H^2(\Omega)}\\ &+\|(u_{n-1}+u_{m-1})\|_{H^2(\Omega)}\|(T_{n-1}-T_{m-1})\|_{H^2(\Omega)}\\ &+\|(v_{n-1}-v_{m-1})\|_{H^2(\Omega)}\|(T_{n-1}+T_{m-1})\|_{H^2(\Omega)}\\ &+\|(v_{n-1}+v_{m-1})\|_{H^2(\Omega)}\|(T_{n-1}-T_{m-1})\|_{H^2(\Omega)}\big).\end{aligned} \tag{50}$$

With a similar approach, we provide the equivalent inequalities for p, u, v, where $M = \sup\{M_T, M_p, M_u, M_v\}$:

$$
\begin{aligned}
\|p_n - p_m\|_{H^2(\Omega)} \leq 2\varepsilon CM \big(& \|u_{n-1} - u_{m-1}\|_{H^2(\Omega)} \|u_{n-1} + u_{m-1}\|_{H^2(\Omega)} \\
& + \|v_{n-1} - v_{m-1}\|_{H^2(\Omega)} \|u_{n-1} + u_{m-1}\|_{H^2(\Omega)} \\
& + \|v_{n-1} + v_{m-1}\|_{H^2(\Omega)} \|u_{n-1} - u_{m-1}\|_{H^2(\Omega)} \\
& + \|v_{n-1} + v_{m-1}\|_{H^2(\Omega)} \|v_{n-1} - v_{m-1}\|_{H^2(\Omega)} \big) \\
& + CRi \|T_n - T_m\|_{H^2(\Omega)}.
\end{aligned} \tag{51}
$$

$$
\begin{aligned}
\|u_n - u_m\|_{H^2(\Omega)} \leq \varepsilon ReCM \big(& \|u_{n-1} - u_{m-1}\|_{H^2(\Omega)} \|u_{n-1} + u_{m-1}\|_{H^2(\Omega)} \\
& + \frac{1}{2} \|v_{n-1} - v_{m-1}\|_{H^2(\Omega)} \|u_{n-1} + u_{m-1}\|_{H^2(\Omega)} \\
& + \frac{1}{2} \|v_{n-1} + v_{m-1}\|_{H^2(\Omega)} \|u_{n-1} - u_{m-1}\|_{H^2(\Omega)} \Big) \\
& + ReC \|p_n - p_m\|_{H^2(\Omega)}.
\end{aligned} \tag{52}
$$

$$
\begin{aligned}
\|v_n - v_m\|_{H^2(\Omega)} \leq \varepsilon ReCM \Big(& \frac{1}{2} \|u_{n-1} - u_{m-1}\|_{H^2(\Omega)} \|v_{n-1} + v_{m-1}\|_{H^2(\Omega)} \\
& + \frac{1}{2} \|u_{n-1} + u_{m-1}\|_{H^2(\Omega)} \|v_{n-1} - v_{m-1}\|_{H^2(\Omega)} \\
& + \|v_{n-1} - v_{m-1}\|_{H^2(\Omega)} \|v_{n-1} + v_{m-1}\|_{H^2(\Omega)} \big) \\
& + ReC \|P_n - P_m\|_{H^2(\Omega)} \\
& + ReRiC \|T_n - T_m\|_{H^2(\Omega)}.
\end{aligned} \tag{53}
$$

Next we show that for small enough ε the entire sequence stay in a small ball.

Lemma 4 (Bounded Sequence). *There exists $\varepsilon_1 > 0$ and $R(\varepsilon_1) < \infty$ for which the sequence is bounded in a ball for all n.*

Proof. We seek to show by strong induction that the sequence is bounded by the ball

$\mathcal{B}_0(R)$ centered at zero with radius R. Hence, let $R(\varepsilon_1)$ be defined such that

$$\|T_0\|, \|T_1\|, \|p_0\|, \|p_1\|, \|u_0\|, \|u_1\|, \|v_0\|, \|v_1\| \leq \frac{R}{2},$$

where we say

$$R = 2\max\{\|T_0\|, \|T_1\|, \|p_0\|, \|p_1\|, \|u_0\|, \|u_1\|, \|v_0\|, \|v_1\|, 1\}$$

to keep R sufficiently large such that each norm is measured in the $H^2(\Omega)$ space. This establishes the base case for induction. Now, we hypothesize by induction that each

$$\|T_{n-1}\|, \|T_{n-2}\|, ..., \|p_{n-1}\|, \|p_{n-2}\|, ..., \|u_{n-1}\|, \|u_{n-2}\|, ..., \|v_{n-1}\|, \|v_{n-2}\|, ... < R$$

where we seek to show that $\|T_n\|, ..., \|v_n\| < R$. Thus, by the above inequalities, it follows that,

$$\begin{aligned} \|T_n - T_1\| \leq \frac{\varepsilon PeCM}{2} \big(&\|(u_{n-1} - u_0)\|\|(T_{n-1} + T_0)\| \\ &+ \|(u_{n-1} + u_0)\|\|(T_{n-1} - T_0)\| \\ &+ \|(v_{n-1} - v_0)\|\|(T_{n-1} + T_0)\| \\ &+ \|(v_{n-1} + v_0)\|\|(T_{n-1} - T_0)\|\big). \end{aligned} \tag{54}$$

By applying the definition of R and the inductive hypothesis it follows that $\|u_{n-1} - u_0\| \leq \frac{3R}{2}$, $\|u_{n-1} + u_0\| \leq \frac{3R}{2}$, $\|v_{n-1} - v_0\| \leq \frac{3R}{2}$, $\|v_{n-1} + v_0\| \leq \frac{3R}{2}$, $\|T_{n-1} - T_0\| \leq \frac{3R}{2}$, and $\|T_{n-1} + T_0\| \leq \frac{3R}{2}$. Hence, we can apply the inequality

$$\|T_n - T_1\| \leq \frac{\varepsilon PeCM}{2} \left(4\left(\frac{3R}{2}\right)\left(\frac{3R}{2}\right)\right)$$

where we select ε_T such that for $\varepsilon < \varepsilon_T$, $\|T_n - T_1\| < \frac{R}{2}$. Hence, let

$$\varepsilon_T = \frac{1}{9PeCMR}$$

and it follows that if $\|T_n - T_1\| < \frac{R}{2}$ then by the reverse triangle inequality

$$|\|T_n\| - \|T_1\|| \leq \|T_n - T_1\| < \frac{R}{2}$$

so

$$\|T_n\| < \frac{R}{2} + \|T_1\| < R.$$

We now proceed by finding the terms $\varepsilon_p, \varepsilon_u, \varepsilon_v$ such that each respective term stays within the ball of radius R. From the pressure inequalities:

$$\begin{aligned} \|p_n - p_1\| \leq 2\varepsilon CM \, (&\|u_{n-1} - u_0\|\|u_{n-1} + u_0\| \\ &+ \|v_{n-1} - v_0\|\|u_{n-1} + u_0\| \\ &+ \|v_{n-1} + v_0\|\|u_{n-1} - u_0\| \\ &+ \|v_{n-1} + v_0\|\|v_{n-1} - v_0\|) \\ &+ CRi\|T_n - T_1\|. \end{aligned} \tag{55}$$

We recall that $\|T_n - T_1\| \leq \frac{9\varepsilon PeCMR^2}{2}$ and again apply the triangle inequality to each norm to obtain:

$$\|p_n - p_1\| \leq 18R^2\varepsilon CM + CRi\frac{9\varepsilon PeCMR^2}{2}.$$

To force $\|p_n - p_1\| < \frac{R}{2}$, we then pick

$$\varepsilon_P = \frac{1}{(36CM + 9C^2RiPeM)R}.$$

For the u velocity inequality, we have:

$$\begin{aligned}\|u_n - u_1\| \leq \varepsilon ReCM \big(&\|u_{n-1} - u_0\|\|u_{n-1} + u_0\| \\ &+ \frac{1}{2}\|v_{n-1} - v_0\|\|u_{n-1} + u_0\| \\ &+ \frac{1}{2}\|v_{n-1} + v_0\|\|u_{n-1} - u_0\|\Big) \\ &+ ReC\|p_n - p_1\|.\end{aligned} \tag{56}$$

So by a similar procedure, we obtain:

$$\varepsilon_u = \frac{1}{(9ReCM + 36ReC^2M + 9ReC^3RiPeM)R}.$$

Finally, For the v velocity inequality, we have:

$$\begin{aligned}\|v_n - v_1\| \leq \varepsilon ReCM \big(&\|v_{n-1} - v_0\|\|v_{n-1} + v_0\| \\ &+ \frac{1}{2}\|v_{n-1} - v_0\|\|u_{n-1} + u_0\| \\ &+ \frac{1}{2}\|v_{n-1} + v_0\|\|u_{n-1} - u_0\|\Big) \\ &+ ReC\|p_n - p_1\| \\ &+ ReRiC\|T_n - T_1\|.\end{aligned} \tag{57}$$

And by the same procedure, we obtain:

$$\varepsilon_v = \frac{1}{(9ReCM + 36ReC^2M + 9ReC^3RiPeM + 9ReRiC^2PeM)R}.$$

We now let $\varepsilon_1 = \inf\{\varepsilon_T, \varepsilon_p, \varepsilon_u, \varepsilon_v\}$ where for all $\varepsilon < \varepsilon_1$,

$$\|T_n\|, \|p_n\|, \|u_n\|, \|v_n\| < R$$

so we conclude by induction that there exists ε_1 such that the sequence remains bounded in a ball of radius R. □

Theorem 3 (**Contraction Mapping).** *The iteration defined by (39) and (40) is a contraction mapping.*

Proof. From the above lemma, we establish by the triangle inequality that each

$$\|T_n + T_m\|, \|p_n + p_m\|, \|u_n + u_m\|, \|v_n + v_m\| \leq 2R.$$

Hence, by the inequality (50) for $\|T_n - T_m\|$, we have:

$$\|T_n - T_m\| \leq \varepsilon PeCMR\|u_{n-1} - u_{m-1}\| + \varepsilon PeCMR\|v_{n-1} - v_{m-1}\| + 2\varepsilon PeCMR\|T_{n-1} - T_{m-1}\|.$$

Similarly, we see that for the other variables:

$$\begin{aligned}\|p_n - p_m\| \leq\ & \varepsilon R(8CM + C^2RiPeM)\|u_{n-1} - u_{m-1}\| \\ & + \varepsilon R(8CM + C^2RiPeM)\|v_{n-1} - v_{m-1}\| \\ & + 2\varepsilon RC^2RiPeM\|T_{n-1} - T_{m-1}\|,\end{aligned}$$

$$\begin{aligned}\|u_n - u_m\| \leq\ & \varepsilon R(3ReCM + 8ReC^2M + ReC^3RiPeM)\|u_{n-1} - u_{m-1}\| \\ & + \varepsilon R(ReCM + 8ReC^2M + ReC^3RiPeM)\|v_{n-1} - v_{m-1}\| \\ & + 2\varepsilon R(ReC^3RiPeM)\|T_{n-1} - T_{m-1}\|,\end{aligned}$$

$$\|v_n - v_m\| \leq \varepsilon R(ReCM + 8ReC^2M + ReC^3RiPeM + ReRiC^2PeM)\|u_{n-1} - u_{m-1}\|$$
$$+ \varepsilon R(3ReCM + 8ReC^2M + ReC^3RiPeM + ReRiC^2PeM)\|v_{n-1} - v_{m-1}\|$$
$$+ 2\varepsilon R(ReC^3RiPeM + ReRiC^2PeM)\|T_{n-1} - T_{m-1}\|.$$

We now consider the product space $S = H^2(\Omega) \times H^2(\Omega) \times H^2(\Omega) \times H^2(\Omega)$ consisting of 4-tuples $X = (X_1, X_2, X_3, X_4)$ of $H^2(\Omega)$ functions with metric defined by:

$$d(X, Y) = \|X_1 - Y_1\| + \|X_2 - Y_2\| + \|X_3 - Y_3\| + \|X_4 - Y_4\| \quad \forall X, Y \in S.$$

Thus, for our set of fluid variables, we establish a new inequality for the sum of differences of index:

$$\|T_n - T_m\| + \|p_n - p_m\| + \|u_n - u_m\| + \|v_n - v_m\| \leq$$
$$\varepsilon RCM(2Pe + 2CRiPe + 4ReC^2RiPe + ReRiCPe)\|T_{n-1} - T_{m-1}\|$$
$$+ \varepsilon RCM(Pe + 8C + CRiPe + 4Re + 16ReC + 2ReC^2RiPe + ReRiCPe)\|u_{n-1} - u_{m-1}\|$$
$$+ \varepsilon RCM(Pe + 8C + CRiPe + 4Re + 16ReC + 2ReC^2RiPe + ReRiCPe)\|v_{n-1} - v_{m-1}\|.$$

Now, define

$$A = \sup(2Pe + 2CRiPe + 4ReC^2RiPe + ReRiCPe,$$
$$Pe + 8C + CRiPe + 4Re + 16ReC + 2ReC^2RiPe + ReRiCPe)$$

such that

$$\|T_n - T_m\| + \|p_n - p_m\| + \|u_n - u_m\| + \|v_n - v_m\| \leq$$
$$3A\varepsilon RCM(\|T_{n-1} - T_{m-1}\| + \|p_{n-1} - p_{m-1}\| + \|u_{n-1} - u_{m-1}\| + \|v_{n-1} - v_{m-1}\|) \tag{58}$$

where we note that $A \lesssim ReRiPe$. Setting $\varepsilon < \frac{1}{3ARCM}$ and defining $F : S \to S$ by

$F(X_{(n-1)}) = X_{(n)}$ for functions $X \in S$ then ensures the Lipschitz condition such that for $X_{(n)} = (T_n, p_n, u_n, v_n)$:

$$d(F(X_{(n-1)}), F(Y_{(n-1)})) = d(X_{(n)}, Y_{(n)}) \leq d(X_{(n-1)}, Y_{(n-1)}). \tag{59}$$

Hence, the iteration is a contraction mapping. □

By a compactness argument, since S is a product space of complete metric spaces it follows that S itself is complete with the metric defined above.
Further, since $F : S \to S$ is a contraction mapping, we thus conclude by the Banach fixed point theorem that F converges to a unique fixed point X^* such that the sequence $X_{(0)}, X_{(1)}, ..., X_{(n)} \to X^*$. It then follows that this X^* is the steady solution to the Navier-Stokes equations for small amplitude forcing and the theorem is proved. □

We now note that since the sequence $X_{(0)}, X_{(1)}, ..., X_{(n)}$ is a convergent, Cauchy sequence, it follows that the inequality of the form (59) is equivalent to the inequality

$$d(X_{(n+1)}, X^*) \leq d(X_{(n)}, X^*) \tag{60}$$

which implies linear convergence to the unique solution X^* for ε which satisfies the Lipschitz condition. From this result, we conclude that the iteration defined by (39) guarantees linear convergence for a sufficiently small amplitude forcing. We now consider a lemma which describes the asymptotic size of solutions as a function of the Re, Pe, and Ri numbers.

Lemma 5 (**Asymptotic Size of Solutions**). *Let* $\|\cdot\|$ *be the* $H^2(\Omega)$ *norm and let*

f be normalized such that $\|f\|_{L^2} = 1$. If $Re \gg Pe$, then for $n \geq 1$,

$$\|v_n\| = \mathcal{O}\left(Re^{2^{n+1}-1} Pe^{2^n} Ri^{2^n} \varepsilon^{2^n-1}\right), \tag{61a}$$

$$\|T_n\| = \mathcal{O}\left(Re^{g_n} Pe^{h_n} Ri^{2^n-1} \varepsilon^{2^n-1}\right) \tag{61b}$$

where

$$g_n = -n + \sum_{j=0}^{n-1} 2^{n-j}$$

and

$$h_n = 1 + n + \sum_{j=1}^{n} 2^{n-j}.$$

Similarly, if $Pe \gg Re$, then

$$\|v_n\| = \mathcal{O}\left(Re^{2^n} Pe^{2^{n+1}-1} Ri^{2^n} \varepsilon^{2^n-1}\right), \tag{62a}$$

$$\|T_n\| = \mathcal{O}\left(Re^{2^n-1} Pe^{2^{n+1}-1} Ri^{2^n-1} \varepsilon^{2^n-1}\right). \tag{62b}$$

Proof. We proceed by induction. Let $X \lesssim Y$ indicate that $X \leq CY$ for some constant C. By recalling the initialization (40) and applying the small amplitude assumption, we establish through Lemma 2 that

$$\|T_0\| \lesssim Pe,$$

$$\|p_0\| \lesssim Ri\|T_0\| \lesssim RiPe,$$

$$\|u_0\| \lesssim Re\|p_0\| \lesssim ReRiPe,$$

$$\|v_0\| \lesssim Re\|p_0\| + Ri\|T_0\| \lesssim ReRiPe.$$

For the $n = 1$ case, we apply the iteration (39) with the small amplitude assumption

and Lemmas 1 and 2 to find

$$\|T_1\| \lesssim \varepsilon Pe\left(\|u_0\|\|T_0\| + \|v_0\|\|T_0\|\right) \lesssim \varepsilon ReRiPe^3,$$

$$\|p_1\| \lesssim \varepsilon\left(\|u_0\|^2 + \|u_0\|\|v_0\| + \|v_0\|^2\right) + Ri\|T_1\|,$$

$$\begin{aligned}\|v_1\| &\lesssim \varepsilon Re(\|v_0\|^2 + \|u_0\|\|v_0\|) + Re\|p_1\| + ReRi\|T_1\| \\ &\quad \varepsilon Re\|v_0\|^2 + ReRiPe\|v_0\|\|T_0\| \\ &\lesssim \varepsilon Re(ReRiPe)^2 + \varepsilon ReRiPe(ReRiPe)Pe.\end{aligned}$$

Thus, if $Re \gg Pe$, we see that $\|v_1\| = \mathcal{O}\left(Re^3Pe^2Ri^2\varepsilon\right)$ and if $Pe \gg Re$ then $\|v_1\| = \mathcal{O}\left(Re^2Pe^3Ri^2\varepsilon\right)$. Hence, the base case is verified. Now, suppose that $Re \gg Pe$. Observe that, due to the additional temperature term in v_n, the asymptotic solution size of $\|u_n\|$ may be bounded by $\|v_n\|$. Now, by applying the inductive hypothesis (61b), we find that

$$\begin{aligned}\|T_{n+1}\| &\lesssim \varepsilon Pe\left(\|u_n\|\|T_n\| + \|v_n\|\|T_n\|\right) \\ &\lesssim \varepsilon Pe\mathcal{O}\left(Re^{2^{n+1}-1}Pe^{2^n}Ri^{2^n}\varepsilon^{2^n-1}\right)\mathcal{O}\left(Re^{g_n}Pe^{h_n}Ri^{2^n-1}\varepsilon^{2^n-1}\right) \\ &= \mathcal{O}\left(Re^{Q}Pe^{M}Ri^{2^{n+1}-1}\varepsilon^{2^{n+1}-1}\right),\end{aligned}$$

where

$$Q = 2^{n+1} - 1 - n + \sum_{j=0}^{n-1} 2^{n-j} = -(n+1) + \sum_{j=0}^{n} 2^{n+1-j}$$

and

$$M = 2^n + 1 + n + \sum_{j=1}^{n} 2^{n-j} = (1+n) + \sum_{j=0}^{n} 2^{n-j} = 1 + (n+1) + \sum_{j=1}^{n+1} 2^{n+1-j}$$

so the inductive result for $\|T_n\|$ holds for $k = n+1$. Further, by applying the inductive hypothesis on $\|v_{n+1}\|$ we see that

$$\begin{aligned}
\|v_{n+1}\| &\lesssim \varepsilon Re\|v_n\|^2 + \varepsilon ReRiPe\|v_n\|\|T_n\| \\
&\lesssim \varepsilon Re\mathcal{O}\left(Re^{2^{n+1}-1}Pe^{2^n}Ri^{2^n}\varepsilon^{2^n-1}\right)^2 \\
&+ \varepsilon ReRiPe\mathcal{O}\left(Re^{2^{n+1}-1}Pe^{2^n}Ri^{2^n}\varepsilon^{2^n-1}\right)\left(Re^{g_n}Pe^{h_n}Ri^{2^n-1}\varepsilon^{2^n-1}\right) \\
&= \mathcal{O}\left(Re^{2^{n+2}-1}Pe^{2^{n+1}}Ri^{2^{n+1}}\varepsilon^{2^{n+1}-1}\right) + \mathcal{O}\left(Re^{2^{n+1}+g_n}Pe^{2^n+g_n}Ri^{2^{n+1}}\varepsilon^{2^{n+1}-1}\right).
\end{aligned}$$

Now, since $g_n = \mathcal{O}(2^n)$ and $Re \gg Pe$, we thus see that

$$\|v_{n+1}\| = \mathcal{O}\left(Re^{2^{n+2}-1}Pe^{2^{n+1}}Ri^{2^{n+1}}\varepsilon^{2^{n+1}-1}\right),$$

verifying the inductive hypothesis.

Now, suppose that $Pe \gg Re$. By applying the inductive hypothesis (62b), we find that

$$\begin{aligned}
&\|T_{n+1}\| \lesssim \varepsilon Pe\left(\|u_n\|\|T_n\| + \|v_n\|\|T_n\|\right) \\
&\lesssim \varepsilon Pe\mathcal{O}\left(Re^{2^n}Pe^{2^{n+1}-1}Ri^{2^n}\varepsilon^{2^n-1}\right)\mathcal{O}\left(Re^{2^n-1}Pe^{2^{n+1}-1}Ri^{2^n-1}\varepsilon^{2^n-1}\right) \\
&= \mathcal{O}\left(Re^{2^{n+1}-1}Pe^{2^{n+2}-1}Ri^{2^{n+1}-1}\varepsilon^{2^{n+1}-1}\right)
\end{aligned}$$

so the inductive result for $\|T_n\|$ holds for $k = n+1$. Further, by applying the inductive

hypothesis on $\|v_{n+1}\|$ we again find that

$$\begin{aligned}
\|v_{n+1}\| &\lesssim \varepsilon Re\|v_n\|^2 + \varepsilon ReRiPe\|v_n\|\|T_n\| \\
&\lesssim \varepsilon Re\mathcal{O}\left(Re^{2^n}Pe^{2^{n+1}-1}Ri^{2^n}\varepsilon^{2^n-1}\right)^2 \\
&+ \varepsilon ReRiPe\mathcal{O}\left(Re^{2^n}Pe^{2^{n+1}-1}Ri^{2^n}\varepsilon^{2^n-1}\right)\mathcal{O}\left(Re^{2^n-1}Pe^{2^{n+1}-1}Ri^{2^n-1}\varepsilon^{2^n-1}\right) \\
&= \mathcal{O}\left(Re^{2^{n+1}+1}Pe^{2^{n+2}-2}Ri^{2^{n+1}}\varepsilon^{2^{n+1}-1}\right) + \mathcal{O}\left(Re^{2^{n+1}}Pe^{2^{n+2}-1}Ri^{2^{n+1}}\varepsilon^{2^{n+1}-1}\right).
\end{aligned}$$

Since $Pe \gg Re$, we conclude that

$$\|v_{n+1}\| = \mathcal{O}\left(Re^{2^{n+1}}Pe^{2^{n+2}-1}Ri^{2^{n+1}}\varepsilon^{2^{n+1}-1}\right),$$

thus verifying the inductive hypothesis and proving the lemma. □

We now introduce a theorem which identifies the maximum laser amplitude as an asymptotic of the Re, Ri, Pe numbers.

Theorem 4 (**Maximum Laser Amplitude**). *If $Re \gg Pe$, then*

$$\varepsilon_{max} = \mathcal{O}\left(Re^{-2}Pe^{-1}Ri^{-1}\right). \tag{63}$$

Similarly, if $Pe \gg Re$, then

$$\varepsilon_{max} = \mathcal{O}\left(Re^{-1}Pe^{-2}Ri^{-1}\right). \tag{64}$$

Proof. Recall from theorem 3 that for the fixed-point iteration to converge, we require

$$\varepsilon < \mathcal{O}\left(A^{-1}R^{-1}\right)$$

for an $R(\varepsilon)$ such that the entire sequence of solutions stay bounded in a ball of size

R. The maximum allowable laser amplitude, then, may be determined by finding the smallest R such that the sequence of solutions stays bounded. This R_{min} will thus be the largest solution in the $H^2(\Omega)$ norm for a given ε. Suppose that $Re \gg Pe$. Then from the above lemma, we observe that the size of the nth iteration may be bounded by the asymptotic $\mathcal{O}\left(Re^{2^{n+1}-1}Pe^{2^n}Ri^{2^n}\varepsilon^{2^n-1}\right)$. Then for the maximum amplitude,

$$\begin{aligned}
\varepsilon_{max} &= \mathcal{O}\left(A^{-1}R_{min}^{-1}\right) \\
&= \inf_{n\in\mathbb{N}} \mathcal{O}\left(Re^{-1}Pe^{-1}Ri^{-1}\left(Re^{2^{n+1}-1}Pe^{2^n}Ri^{2^n}\varepsilon_{max}^{2^n-1}\right)^{-1}\right) \\
&= \inf_{n\in\mathbb{N}} \mathcal{O}\left(Re^{2^{n+1}}Pe^{2^n+1}Ri^{2^n+1}\varepsilon_{max}^{2^n-1}\right)^{-1}
\end{aligned}$$

so

$$\varepsilon_{max}^{2^n} = \mathcal{O}\left(Re^{-2^{n+1}}Pe^{-2^n-1}Ri^{-2^n-1}\right)$$

and thus

$$\varepsilon_{max} = \inf_{n\in\mathbb{N}} \mathcal{O}\left(Re^{-2}Pe^{-\frac{2^n-1}{2^n}}Ri^{-\frac{2^n-1}{2^n}}\right) = \mathcal{O}\left(Re^{-2}Pe^{-1}Ri^{-1}\right).$$

Now, suppose that $Pe \gg Re$. By again applying Lemma 5, we observe that the size of the nth iteration may now be bounded by the asymptotic $\mathcal{O}\left(Re^{2^n}Pe^{2^{n+1}-1}Ri^{2^n}\varepsilon^{2^n-1}\right)$. Then for the maximum amplitude,

$$\begin{aligned}
\varepsilon_{max} &= \mathcal{O}\left(A^{-1}R_{min}^{-1}\right) \\
&= \inf_{n\in\mathbb{N}} \mathcal{O}\left(Re^{-1}Pe^{-1}Ri^{-1}\left(Re^{2^n}Pe^{2^{n+1}-1}Ri^{2^n}\varepsilon_{max}^{2^n-1}\right)^{-1}\right) \\
&= \inf_{n\in\mathbb{N}} \mathcal{O}\left(Re^{2^n+1}Pe^{2^{n+1}}Ri^{2^n+1}\varepsilon_{max}^{2^n-1}\right)^{-1}
\end{aligned}$$

so

$$\varepsilon_{max}^{2^n} = \mathcal{O}\left(Re^{-2^n-1}Pe^{-2^{n+1}-1}Ri^{-2^n-1}\right)$$

and thus

$$\varepsilon_{max} = \inf_{n\in\mathbb{N}} \mathcal{O}\left(Re^{-\frac{2^n-1}{2^n}} Pe^{-2} Ri^{-\frac{2^n-1}{2^n}}\right) = \mathcal{O}\left(Re^{-1} Pe^{-2} Ri^{-1}\right).$$

□

In Chapter IV, we compare this analysis to numerical results for the maximum laser amplitude in convergent iterations for homogeneous Dirichlet boundary conditions. In the following section, we introduce the numerical techniques by which we may develop numerical algorithms to take advantage of the convergence of the fixed-point method.

3.2 Numerical Algorithms

In Section 2.2, we described the fundamental approaches to solving a Poisson boundary value problem on a finite domain using numerical methods. In this section, we describe the implementation of these numerical Poisson solvers to find convergent solutions to the steady-state Navier–Stokes problem defined in (4). We then introduce the approach to solving the same problem using a Newton's method algorithm, wherein we compare the merits of the two in computational cost and convergence rate. Finally, we will describe a numerical continuation technique to increase the domain of solutions which we can determine from both of these aforementioned algorithms.

3.2.1 Poisson Solver Implementation

3.2.1.1 Procedure

Recall that, as described in Chapter II, we may numerically solve a classical Poisson boundary value problem of the form (24), (26), (34) by discretizing the domain Ω into a grid of uniform spacing h and solving for the approximate values of the

function u at each of the grid points. Define $N = \frac{1}{h} + 1$ to be the number of grid points in one spatial direction and let Ω_D be the grid which is the discretization of the domain Ω as a function of the spacing h. We now suppose that each constant arising in the iteration (39) $Re, Ri, Pe, \varepsilon,$ and c are defined by the user based on the laser and fluid properties and the normalized laser forcing takes the Gaussian form $f(x, y) = e^{-c(x^2+y^2)}$. We further suppose that each fluid variable has associated classical boundary conditions of the Dirichlet, Neumann, or mixed type. To begin the process of computing numerical representations of the iteration (39), we begin by computing the initial temperature T_0 through the Poisson equation (40d) where f is defined over the grid Ω_D. This is accomplished through the discrete Poisson solvers described in section 2.2 according to the imposed temperature boundary condition where T_0 is a discrete vector representing the numerical solution over the grid Ω_D. We then proceed to calculate the pressure p_0 through equation (40c), where the derivative term in temperature is a finite difference approximation of the y-direction gradient component. This finite difference approximation is calculated through the use of a discrete gradient operator D_y which utilizes a centered difference approximation to the derivative of the form (29) with a second order forward and backward difference along the boundaries. A similar matrix D_x is constructed for the x-component of the gradient. With p_0 determined, We then proceed to solve for u_0 and v_0 through the equations (40b) and (40a) with the respective u, v boundary conditions.

With the initialization to the iteration now fully determined, we proceed to calculate each of the numerical approximations to the fluid variables (T_n, p_n, u_n, v_n) as defined in the iteration (39). The second derivative approximation matrices are denoted $D_{xx}, D_{yy}, D_{xy} = D_{yx}$ where they utilize a second-order centered-difference formula as described in (22). By defining the operation $[*]$ to be pointwise multiplication, the

discrete version of the iteration (39) then becomes

$$\Delta u_n = Re\left(u_{n-1} * D_x u_{n-1} + v_{n-1} * D_y u_{n-1} - D_x p_n\right), \tag{65a}$$

$$\Delta v_n = Re\left(u_{n-1} * D_x v_{n-1} + v_{n-1} * D_y v_{n-1} - D_y p_n - RiT_n\right), \tag{65b}$$

$$\begin{aligned}\Delta p_n = {} & u_{n-1} * D_{xx} u_{n-1} + (D_x u_{n-1}) * (D_x u_{n-1}) + v_{n-1} * D_{xy} u_{n-1} + 2(D_x v_{n-1}) * (D_y u_{n-1}) \\ & + u_{n-1} * D_{yx} v_{n-1} + v_{n-1} * D_{yy} v_{n-1} + (D_y v_{n-1}) * (D_y v_{n-1}) - RiD_y T_n,\end{aligned} \tag{65c}$$

$$\Delta T_n = Pe\left(u_{n-1} * D_x T_{n-1} + v_{n-1} * D_y T_{n-1} - \varepsilon f\right). \tag{65d}$$

By applying this discrete iteration, we are thus able to calculate the numerical fluid variables over the grid Ω_D at each step n. To determine if a fixed-point solution is reached, we establish a stopping criteria δ such that if the Cauchy error of each fluid variable falls below δ then we claim that the algorithm converges. Since $H^2(\Omega)$ is a complete metric space, the Cauchy error must therefore tend to zero for a convergent solution. We thus check to see if the product space metric satisfies

$$\|T_n - T_{n-1}\|_{H^2} + \|p_n - p_{n-1}\|_{H^2} + \|u_n - u_{n-1}\|_{H^2} + \|v_n - v_{n-1}\|_{H^2} < \delta \tag{66}$$

and if so, we claim that the variables (T_n, p_n, u_n, v_n) represent the unique steady-state solution. For the discrete variables (T_n, p_n, u_n, v_n), we approximate the H^2 norm by taking the vector 2-norm in $\mathbb{R}^{(N+1)^2}$. If this stopping criterion is not satisfied after a predetermined number of iterations, then we claim that the iteration diverges for the chosen laser amplitude ε. The exact values of δ and the maximum number of iterations depend on the desired accuracy of the solution and an analysis on the numerical speed of convergence.

3.2.1.2 Computational Complexity

At each step in the discrete iteration (65), we perform a series of four Poisson solves for the fluid variables over the grid Ω_D. In analyzing the total computational cost of the procedure, we are interested in determining the asymptotic as function of the grid spacing h. During each substep, we must account for the cost of evaluating the right hand side over Ω_D in the discrete Poisson solver along with the cost of solving the linear system $\mathbf{A}\mathbf{u}_D = \mathbf{f}$ which represents the discrete Poisson boundary value problem. By observing the calculations in the iteration (40), we see that the matrix-vector computations in the sparse discrete gradients cost the number of non-zero elements which come in at $\mathcal{O}(N^2)$ and the pointwise-matrix products in the fluid variables also cost $\mathcal{O}(N^2)$. Further, since the $N^2 \times N^2$ $\mathbf{A}$ matrix for the linear system defined for the discrete Poisson problem is a banded matrix, the cost to populate it is at worst $\mathcal{O}(N^2)$. To solve a linear system of the form $\mathbf{A}\mathbf{u}_D = \mathbf{f}$ with a $N^2 \times N^2$ matrix, the canonical Gaussian elimination algorithm costs $\mathcal{O}(N^6)$ to compute. We now take advantage of the sparsity property of the $\mathbf{A}$ matrix wherein algorithms exist to solve sparse linear systems for as low as $\mathcal{O}(N^2 \log N^2)$. We thus compare three separate algorithms for solving sparse linear systems: MATLAB's *mldivide*, MATLAB's *mldivide* for sparse matrices, and a fast Poisson solver developed by Langston [30] which uses FFT methods in a sparse LU decomposition to solve the linear system. MATLAB determines which sparse matrix factorization algorithm to use based on the matrix properties [31], where an optimal solver will cost $\mathcal{O}(N^2 \log N^2)$. Figure 5 compares the time to run for these three algorithms as a function of the grid size.

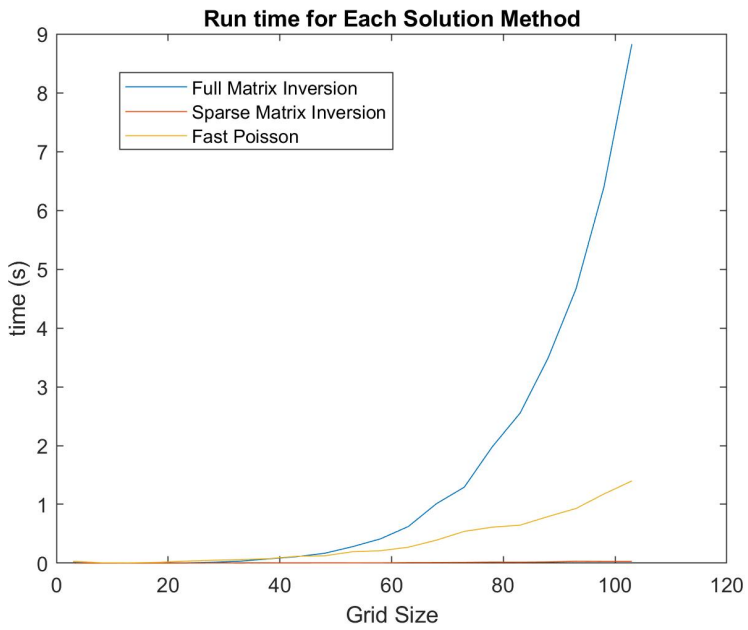

Figure 5: A comparison of the timing cost for three different algorithms in computing a Poisson solver for Dirichlet conditions. The MATLAB sparse solver appears to be the fastest as the grid size grows asymptotically large.

This figure indicates that the MALTAB sparse matrix algorithm performs the Poisson solve the fastest for asymptotically large N and we thus use this algorithm in the Poisson iteration scheme. In order to estimate the asymptotic of the computational cost, Figure 6 provides a plot of the sparse algorithm's timing for both Dirichlet and Neumann problems versus an $\mathcal{O}(N^2 \log N^2)$ asymptotic. Based on the $\mathcal{O}(N^2 \log N^2)$ convergence observed in Figure 6, it then follows that the overall computational complexity comes in at approximately $\mathcal{O}(N^2 \log N^2)$ which includes each of the steps in the numerical iteration. This is significant since we now have an avenue to compute solutions to a system of nonlinear pdes by a convergent iteration which asymptotically costs the same as an inexpensive matrix inversion algorithm. The next subsection explores the implementation of a Newton solver approach, where we compare the computational cost between this iterative algorithm and the Newton's method algorithm.

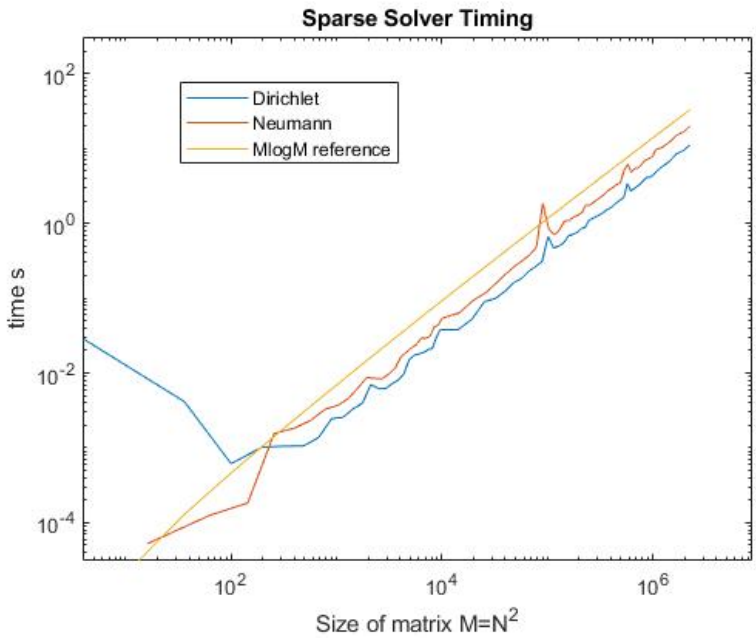

Figure 6: A log-log plot of the timing cost as a function of matrix size $M = N^2$ for the MATLAB sparse solver in a Dirichlet and a Neumann problem. The timing asymptotic is compared to a $\mathcal{O}(N^2 \log N^2)$ asymptotic where they agree as M grows asymptotically large.

3.2.2 Newton's Method Implementation

Recall that in Section 2.2, we determined how Newton's method can be applied to solve nonlinear algebraic systems of equations. With the method itself cannot be directly used to solve systems of partial differential equations, we may apply a discretization to the derivative terms which transforms a system of pdes to a system on nonlinear algebraic equations. Therefore, we suppose that we apply the same finite discretization Ω_D to the solution domain. The governing steady-state equations (4) then take on their discrete analog where each differentiation operator takes on the

form D_x, D_y, $D_x x$, D_{xy}, D_{yy}, respectively. Let the vector $\mathbf{x} \in \mathbb{R}^{4N^2}$

$$\mathbf{x} = \begin{bmatrix} \mathbf{T} \\ \mathbf{p} \\ \mathbf{u} \\ \mathbf{v} \end{bmatrix} \tag{67}$$

represent the collated fluid variables over the discrete grid. At each grid point, there exists a governing equation for the finite difference discretization of the system of coupled Poisson equations (4). By following the grid enumeration presented in Figure 3, we let the vector $\mathbf{F}(\mathbf{x}) \in \mathbb{R}^{4N^2}$ represent these governing equations in the discrete Poisson formulation where each of the four Poisson equations are stacked in a vector format. To perform the Newton step, we now have to consider the Jacobian matrix

$$\mathbf{J} = \begin{pmatrix} \frac{\partial \mathbf{F}_1}{\partial \mathbf{x}_1} & \frac{\partial \mathbf{F}_1}{\partial \mathbf{x}_2} & \cdots & \frac{\partial \mathbf{F}_1}{\partial \mathbf{x}_{4N^2}} \\ \frac{\partial \mathbf{F}_2}{\partial \mathbf{x}_1} & \ddots & \cdots & \\ \vdots & \ddots & \cdots & \\ \frac{\partial \mathbf{F}_{4N^2}}{\partial \mathbf{x}_1} & \cdots & \frac{\partial \mathbf{F}_{4N^2}}{\partial \mathbf{x}_{4N^2}} & \end{pmatrix}. \tag{68}$$

Based on the finite difference discretization for the Poisson equations discussed previously, each $\mathbf{F}_k$ is a linear combination of the discretized fluid variables $\mathbf{x}$. By employing the numerical Poisson solvers, we can therefore determine this linear relationship between the governing equations and the fluid variables in the finite difference formulation. Once these linear coefficients are extracted, they populate the Jacobian matrix as defined in equation (68). The Newton solver then makes the iteration

$$\mathbf{x}_{k+1} = \mathbf{x}_k - \mathbf{J}^{-1}\mathbf{F}(\mathbf{x}_k)$$

where, in practice, the inverse Jacobian isn't directly computed and we instead utilize a linear system solver. In populating the Jacobian, we require $\mathcal{O}(N^4)$ function evaluations. Further, applying canonical Gaussian elimination on the Jacobian linear system requires $\mathcal{O}(N^6)$ operations. While the Jacobian is inherently sparse, it loses the banded structure that the Poisson solver matrices contain. Consequently, a sparse solver on the Jacobian won't yield nearly as optimal a computational cost as a similarly sized banded matrix would. The best estimate for the factorization of a nonbanded, sparse matrix would be $\mathcal{O}(N^4)$ [32]. Therefore, we conclude that the Newton's method iterations cost between $\mathcal{O}(N^4)$ and $\mathcal{O}(N^6)$, indicating a much higher computational cost as compared to the fixed-point solver. A sparsity pattern of the Jacobian for $N = 51$ with homogeneous Dirichlet boundary conditions is provided in Figure 7.

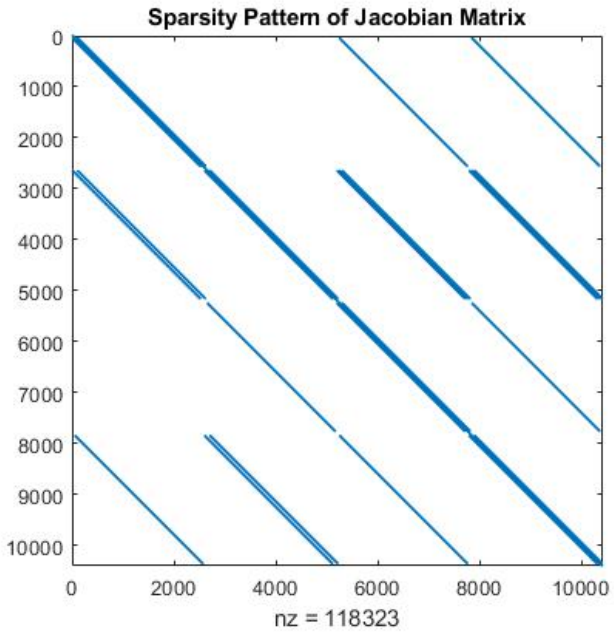

Figure 7: A sparsity plot depicting the nonzero elements of the Jacobian matrix for h=1/50 and homogeneous Dirichlet boundary conditions. Due to the coupled nature of the governing equations, the Jacobian loses a banded structure and it thus more computationally complex to invert in the Newton iteration compared to the Poisson solvers in the fixed-point iteration.

3.2.3 Numerical Continuation

In attempting to find an iterative solution to a nonlinear system of equations, we are often faced with an inability to find a sufficient initial guess which leads to a convergent solution. By applying the process of continuation, however, we are able to successively solve easier problems which lead to the solution to the original problem. As described in Novak [33], we illustrate this by supposing that we seek to find the root $\mathbf{x}^*$ to the function $f(\mathbf{x})$. We are unable to directly find the root with our currently employed method, but we are able to find the root $\tilde{\mathbf{x}}$ for a simpler function $g(\mathbf{x})$. Then, if the two functions are homotopic, there exists a homotopy $h(\mathbf{x})$ which continuously deforms $g(\mathbf{x})$ into $f(\mathbf{x})$ within the same topological space. By tracking the values of the homotopy, we are able to start with the solution to the easier problem and end with the solution to the desired problem.

Numerical continuation offers a simple yet practical procedure of the same nature which can be applied to the iterative Poisson solver and Newton's method algorithms discussed previously. Let $X_n = (T_n, p_n, u_n, v_n)$ be the nth iteration of the fluid variables defined in the Poisson iteration (65). We then suppose that we seek to find the fixed point X^* for the laser forcing amplitude ε. If, given an initialization X_0, the iteration is unable to converge, we then apply a numerical continuation procedure. Further suppose that we know the initialization $\tilde{X}_0$ converges to the solution $\tilde{X}^*$ for a different laser forcing amplitude ε_0. The continuation procedure then introduces a $\delta\varepsilon$ parameter which is added to the known solution amplitude ε_0 to define a new problem with amplitude $\tilde{\varepsilon} = \varepsilon_0 + \delta\varepsilon$. We then assign the initialization for this new problem to be the known solution to the previous problem. That is, we assign

$$\tilde{X}_0 \to \tilde{X}^* \tag{69}$$

to be the initialization for the problem with laser amplitude $\tilde{\varepsilon}$ and repeat the procedure with another $\delta\epsilon$ step until the initialization $\tilde{X}_0$ leads to the solution X^* for the problem with amplitude ε. This procedure thus operates by successively improving the iteration's initialization until it falls within a convergent region.

In practice, the continuation step size $\delta\varepsilon$ usually varies as a function of the previous step sizes. For example, we may select $\delta\varepsilon$ such that the next amplitude is a 10% increase from the previous step until the desired amplitude is reached. A more effective approach, however, is to allow the step size to adapt based on the success or failure of the previous solution attempt. This is referred to as *adaptive continuation*. If the previous initialization led to a convergent solution, the next continuation step size $\delta\varepsilon$ is increased by some factor (e.g. 2). If the previous initialization failed to lead to a convergent solution, the step size then decreases by a factor (e.g. 1/2). With this adaptive continuation approach, the step size effectively corrects itself to grow or decrease depending on the difficulty of finding a sufficient initialization to lead to a solution. By picking some amplitude ε_0 which has an initialization leading to convergence and some initial step size $\delta\varepsilon_0$, we are thus able to determine solutions of any amplitude ε assuming a homotopy exists between the initial and desired solutions. In the following chapter, we will see examples of this continuation approach leading to previously unknown solutions, as well as examples in which continuation fails to find a solution of a desired amplitude.

IV. Results and Analysis

In the previous two chapters, we have introduced the necessary theory and methodology by which to achieve informative numerical results for laser-fluid interaction. This chapter therefore serves the twofold purpose of providing these numerical results and elucidating their mathematical and physical significance. In the following sections, we will describe the solution profiles for a homogeneous Dirichlet, experimental Dirichlet, and slip boundary value problem; the relationship between the fluid constants Re, Ri, Pe and the maximum calculable laser amplitude; and the bifurcation diagrams for convergent solutions in the fixed-point and Newton's method solvers.

4.1 Solution Profiles

We now seek to understand the physical nature of the steady-state solutions defined in the iteration (39) for different boundary conditions on the fluid variables. To begin, we consider the various fluid and laser constants which are required to simulate solutions. For a characteristic length scale L, characteristic velocity scale U, force due to gravity g, kinematic viscosity ν, and thermal diffusivity μ, the Reynolds, Peclet, and Richardson numbers are respectively defined as

$$Re = \frac{UL}{\nu}, \quad Pe = \frac{UL}{\mu}, \quad Ri = \frac{gL}{U^2}. \tag{70}$$

Akers and Reeger [34] provide a discussion on the relationship between these parameters and the laser beam characteristics. In practice, the person running the simulation specifies these constants based on the laser and the fluid it propagates through. In these results, we set the Peclet number $Pe = Re$ equal to the Reynolds number, and we set the Richardson number $Ri = 10Re$ to be an order of magnitude larger than

the Reynolds number. For the normalized laser forcing $f(x, y) = e^{-c(x^2+y^2)}$, we pick $c = 50$ to represent rapid Gaussian decay from the origin. This parameter, however, can also be changed based on the exact laser specifications. A surface plot of the normalized laser forcing is provided in Figure 8 for a grid spacing of $h = \frac{1}{50}$.

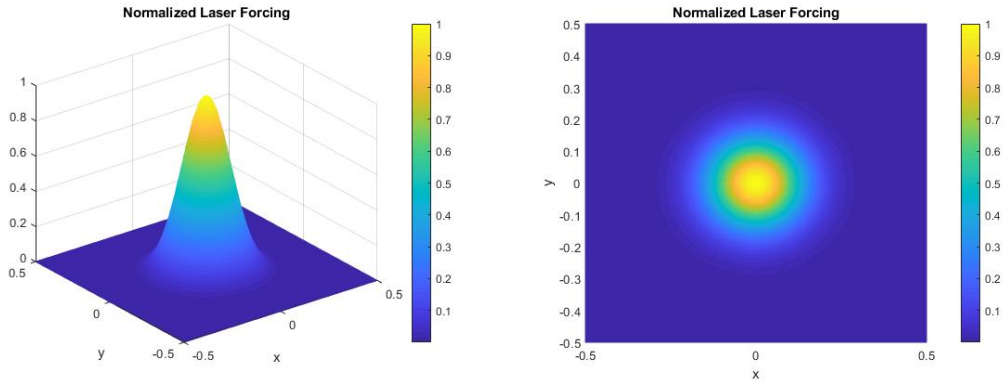

Figure 8: A surface plot of the laser forcing across the domain. The grid spacing is $h = \frac{1}{50}$. The forcing rapidly decays from the origin in a Gaussian shape.

We now introduce the solutions for the fluid variables (T, p, u, v) over the finite grid for three different boundary value problems.

4.1.1 Homogeneous Dirichlet

The first boundary value problem we consider is the simplest. In the homogeneous Dirichlet case, each fluid variables takes on a value of zero along the boundary such that

$$\begin{cases} T(x, y) = 0, & (x, y) \in \partial\Omega, \\ p(x, y) = 0, & (x, y) \in \partial\Omega, \\ u(x, y) = 0, & (x, y) \in \partial\Omega, \\ v(x, y) = 0, & (x, y) \in \partial\Omega. \end{cases} \tag{71}$$

To simulate this boundary value problem, we assign $Re = Pe = 100$ and $Ri = 1000$ with a grid spacing of $h = \frac{1}{50}$ and a laser amplitude of $\varepsilon = 10^{-7}$. These values are selected based on the convergence properties of the iteration, which will be discussed in Section 4.3. Figure 9 provides a streamline plot and Figures 10–13 provide the steady-state solutions for each of the fluid variables.

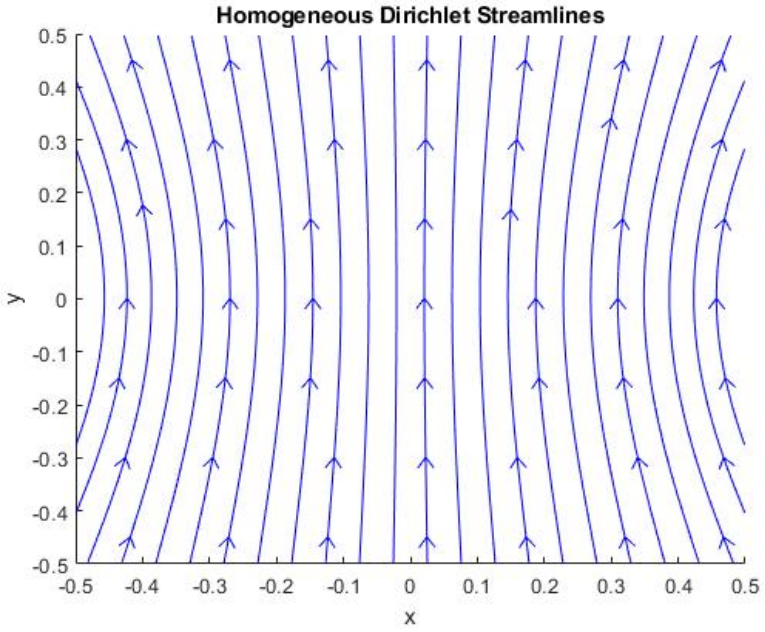

Figure 9: Streamline plot for the homogeneous Dirichlet boundary condition. We observe that the fluid tends to move upward until reaching a stopping point along the boundary. Further, solutions tend to move towards the edges of the domain as they travel vertically.

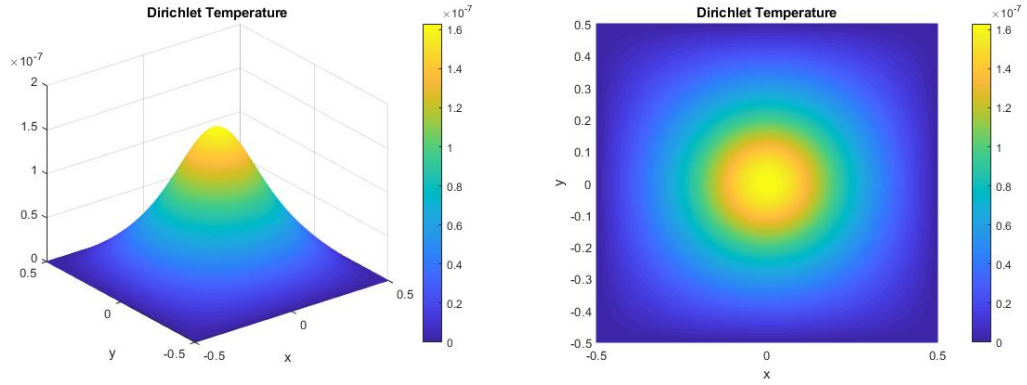

Figure 10: The temperature defined over the grid for homogeneous Dirichlet boundary conditions. We observe that the temperature exhibits a similar shape as the laser forcing, where the boundary conditions induce symmetry over the domain.

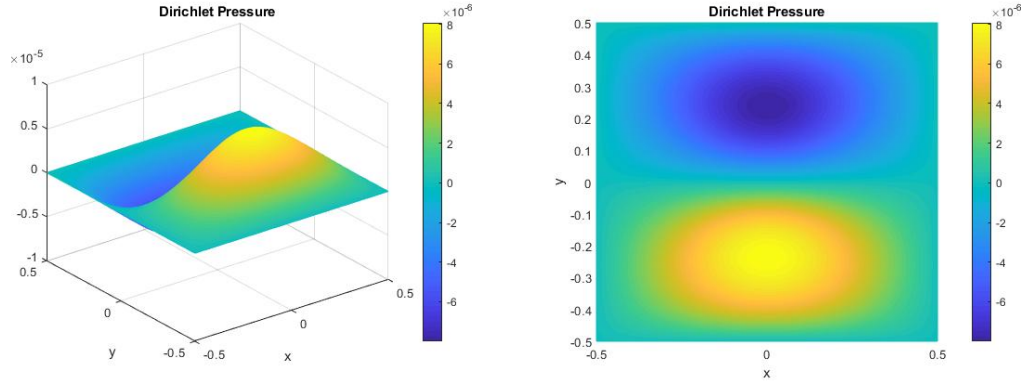

Figure 11: The pressure defined over the grid for homogeneous Dirichlet boundary conditions. We notice the odd symmetry across the x-axis where a pressure buildup forces the vertical velocity to zero along the boundaries.

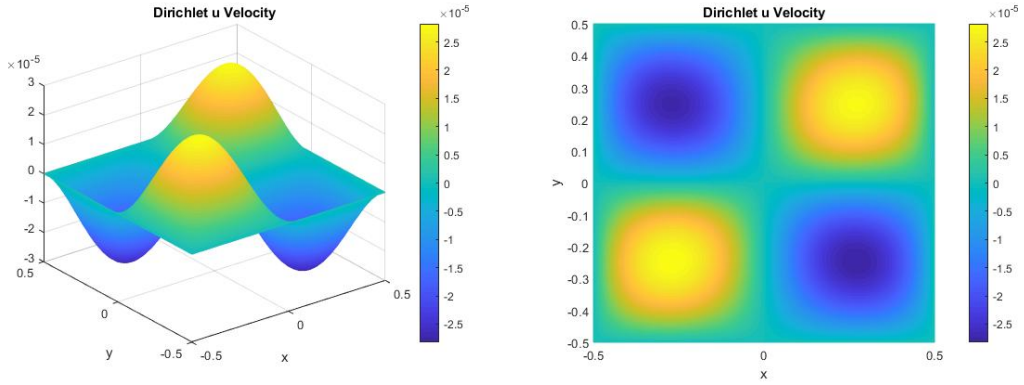

Figure 12: The x-direction velocity u defined over the grid for homogeneous Dirichlet boundary conditions. Based on this profile and the streamlines, we observe that the u velocity induces fluid movement from the edges of the domain to the center of the domain towards the bottom, and it induces movement toward the edges near the top of the domain.

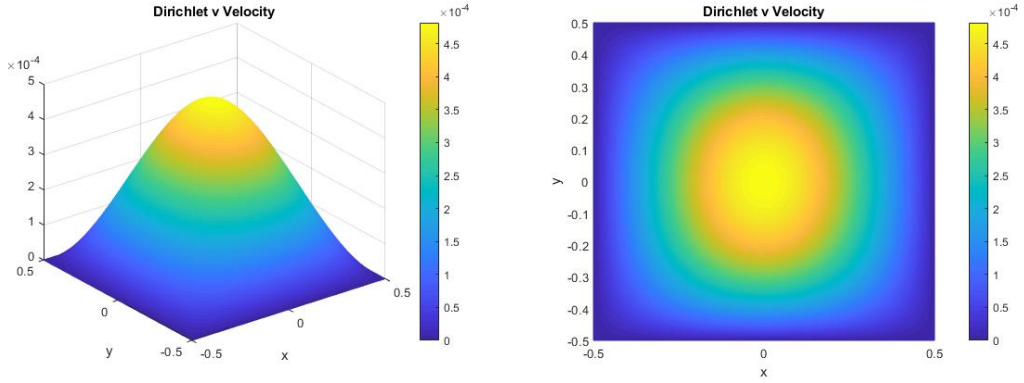

Figure 13: The y-direction velocity v defined over the grid for homogeneous Dirichlet boundary conditions. This velocity takes on a similar shape to the temperature, where the fluid moves upward with highest velocity near the laser in the center.

These results provide an insightful understanding of the fluid behavior within the domain Ω for this specific boundary value problem. While the homogeneous Dirichlet case isn't necessarily a physically valid boundary condition, we can infer

general trends in the fluid variables. We notice immediately that the temperature and vertical velocity are strictly positive on the interior of the domain with decay from the origin towards the boundaries. Further, based on the streamlines, we notice that the fluid tends to move towards the center near the bottom boundary, and towards the edges nearer the top boundary. Thus suggests some prognostication of circulatory flow within the domain, which may inform the behavior of more physical boundary conditions.

4.1.2 Slip Boundary Conditions

We now consider the more physical boundary value problem consisting of slip boundary conditions. We restate these conditions described by equation (20) as

$$\begin{cases} v(x,y) = 0, \quad \frac{\partial u(x,y)}{\partial y} = 0, & (x,y) \in \partial\Omega_{\text{top}} \cup \partial\Omega_{\text{bottom}}, \\ u(x,y) = 0, \quad \frac{\partial v(x,y)}{\partial x} = 0, & (x,y) \in \partial\Omega_{\text{left}} \cup \partial\Omega_{\text{right}}, \\ T(x,y) = 0, & (x,y) \in \partial\Omega, \\ P(x,y) = 0, & (x,y) \in \partial\Omega. \end{cases}$$

Recall that in our discussion in Section 2.2 we described the physicality of the slip boundary condition in modeling a closed box. Figure 14 provides a streamline plot and Figures 15-18 provide the steady-state solutions for the fluid variables in the slip boundary value problem.

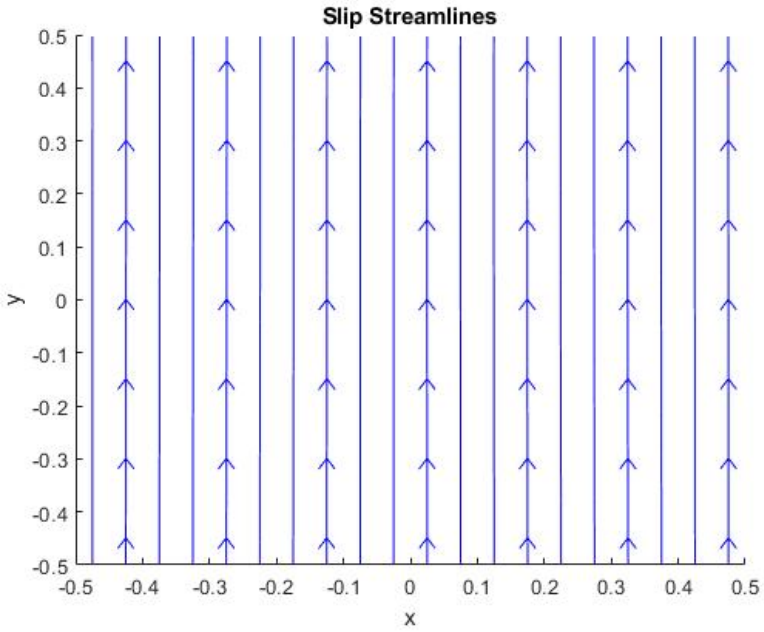

Figure 14: Streamline plot for the slip boundary condition. We see that the fluid tends to move upward before coming into contact with the boundary.

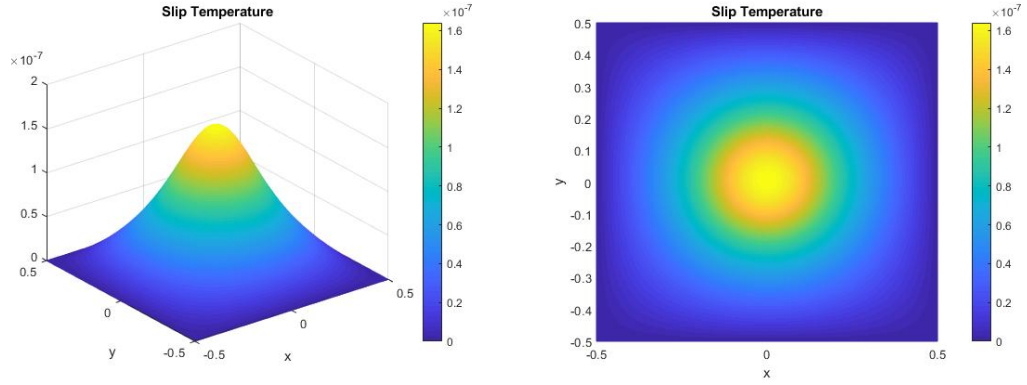

Figure 15: The temperature defined over the grid for Slip boundary conditions. Based on the symmetry and the zero boundary values, the temperature again exhibits a similar shape to that of the homogeneous Dirichlet boundary value problem.

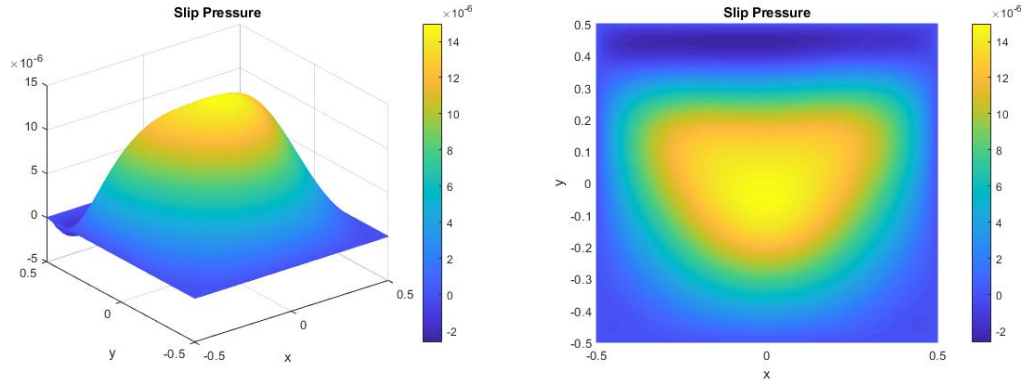

Figure 16: The pressure defined over the grid for slip boundary conditions. We notice that the pressure is large towards the center where the vertical velocity is highest.

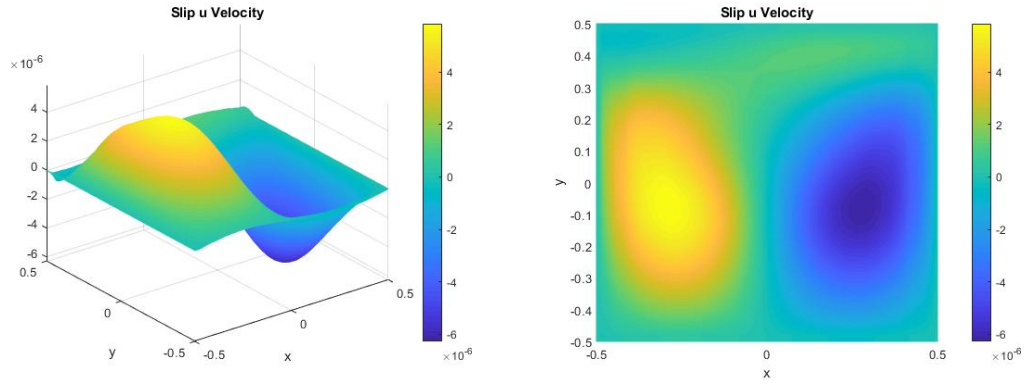

Figure 17: The x-direction velocity u defined over the grid for slip boundary conditions. Based on this profile, we observe that the u velocity induces fluid movement from the edges of the domain to the center, albeit at a much lower magnitude compared to the vertical velocity.

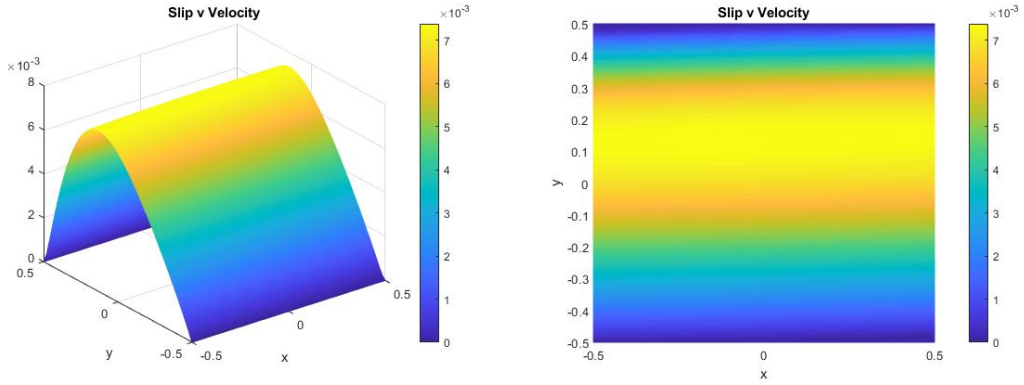

Figure 18: The y-direction velocity v defined over the grid for slip boundary conditions. This velocity is symmetric about the y-axis, suggesting a steady-state velocity which is independent of horizontal position relative to the laser.

These results endow several notable fluid behaviors in the slip boundary value problem. Due to the underlying physical assumption inherit to the slip condition, no fluid is allowed to escape the box such that the normal velocity to each boundary surface is zero. This leads to a tendancy for the fluid to move towards the top of the domain before stopping. We note that the vertical velocity v reaches its maximum at a vertical location slightly above the origin. This is due to the gravity effect implicit in the Richardson number, which skews the velocity away from the center. Overall, these results suggest a movement of fluid towards the top boundary where the horizontal and vertical velocities both tend to zero, similar to a no-slip condition.

4.1.3 Experimental Boundary Conditions

We now recall the brief discussion contained in Chapter II surrounding the possibilities of implementing an experimental boundary value problem such that the fluid is now able to escape out of the top and bottom boundaries. That is, we may specify some specific Dirichlet profile for the velocity along the top and bottom boundaries such that the fluid is free to move into and out of the domain. Determining adequate

boundary profiles to represent a physical solution is a difficult problem, and likely requires experimental data to inform on such a boundary condition. We now offer a superficial construction of an example experimental boundary value problem. Suppose that each fluid variable's boundary value is of the homogeneous Dirichlet type except for the top and bottom of the temperature, vertical, and horizontal velocity. We then assume that the temperature and vertical velocity take on a sinusoidal profile along the top boundary of the form

$$g(x) = \alpha \cos(\pi x) \tag{72}$$

for some positive constant α. This form is selected to ensure zero values at the corner points such that the boundary conditions are continuous from the sides to the top. We then set the vertical velocity along the bottom to be equal to the top boundary condition such that an equal amount of fluid enters and leaves the domain. To induce a circular motion of fluid into and out of the domain, we pick the horizontal velocity at the top and bottom boundaries to take on the value

$$g_u(x) = \pm\beta \sin(2\pi x) \tag{73}$$

for a positive constant β. In establishing a boundary of this type, we further assume that the experimental setup allows for the boundary temperature to remain in a steady-state. Then, by picking $\beta = \alpha_v = \varepsilon ReRi$ and $\alpha_T = \varepsilon$ based on the governing

steady-state equations (4), we obtain the experimental boundary conditions

$$\begin{cases} T(x,y) = 0, \quad v(x,y) = 0, & (x,y) \in \partial\Omega_{\text{left}} \cup \partial\Omega_{\text{right}}, \\ T(x,y) = 0, & (x,y) \in \partial\Omega_{\text{bottom}}, \\ T(x,y) = -\varepsilon \cos(\pi x), & (x,y) \in \partial\Omega_{\text{top}}, \\ v(x,y) = -\varepsilon ReRi \cos(\pi x), & (x,y) \in \partial\Omega_{\text{top}} \cup \partial\Omega_{\text{bottom}}, \\ u(x,y) = \varepsilon ReRi \sin(2\pi x), & (x,y) \in \partial\Omega_{\text{top}}, \\ u(x,y) = -\varepsilon ReRi \sin(2\pi x), & (x,y) \in \partial\Omega_{\text{bottom}}, \\ u(x,y) = 0, & (x,y) \in \partial\Omega_{\text{left}} \cup \partial\Omega_{\text{right}}, \\ P(x,y) = 0, & (x,y) \in \partial\Omega. \end{cases} \tag{74}$$

Figure 19 provides a streamline plot and Figures 20–23 provide the solutions for each of the fluid variables in the experimental boundary case.

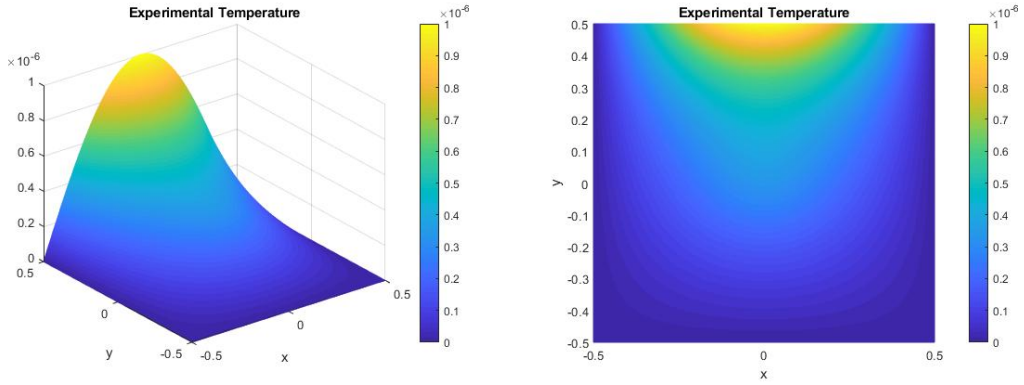

Figure 20: The temperature defined over the grid for the experimental boundary condition. This temperature maintains a profile along the top boundary which matches the vertical velocity such that the fluid moving the fastest out of the domain is also the highest temperature.

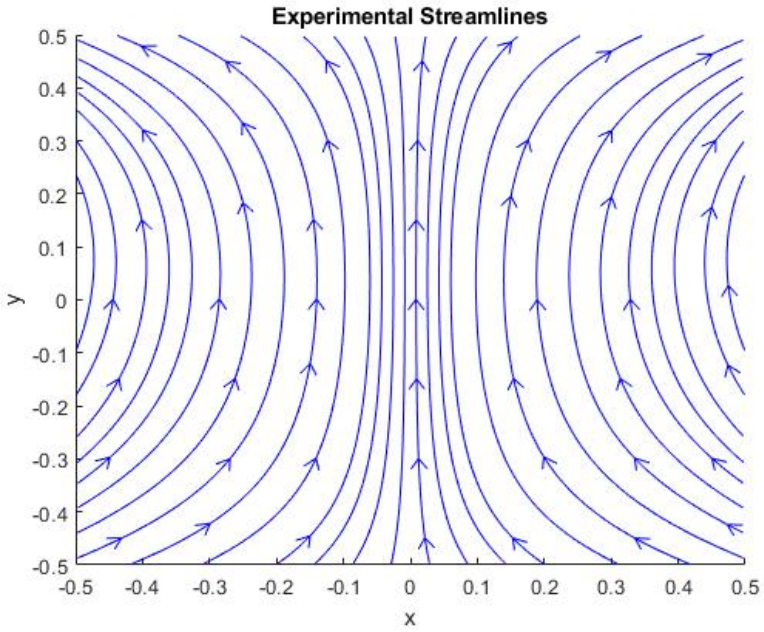

Figure 19: Streamline plot for the experimental boundary condition. We notice immediately that the fluid enters and leaves the domain in a circular fashion. This suggests a tendency for the fluid to move upward and to the sides of the domain in the steady-state.

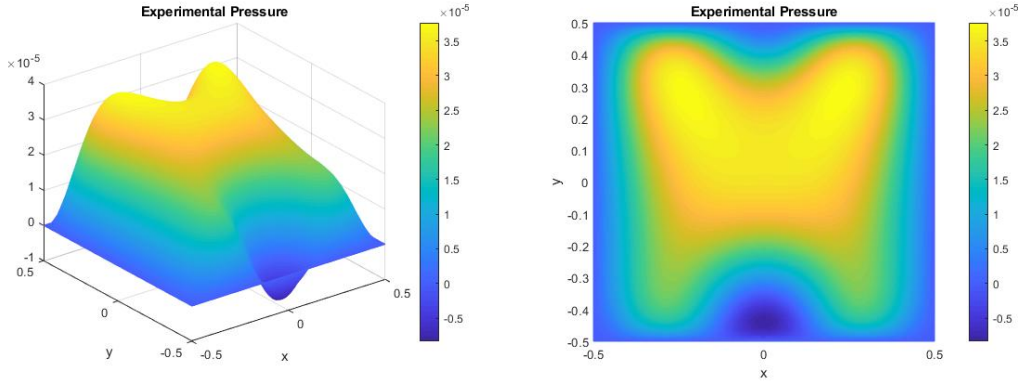

Figure 21: The pressure defined over the grid for the experimental boundary condition. Notice that the pressure is largest in magnitude towards the upper half of the domain where fluid circulates outward.

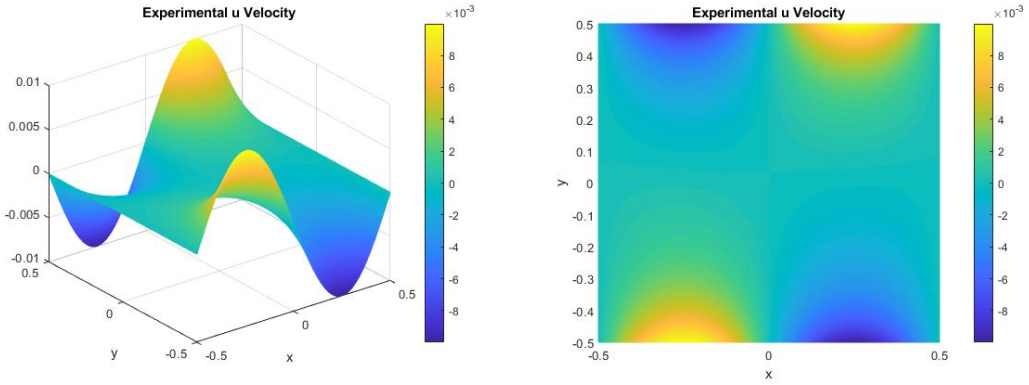

Figure 22: The x-direction velocity u defined over the grid for the experimental condition. Notice the odd symmetry across both axes which induces the fluid movement seen in the streamline plot.

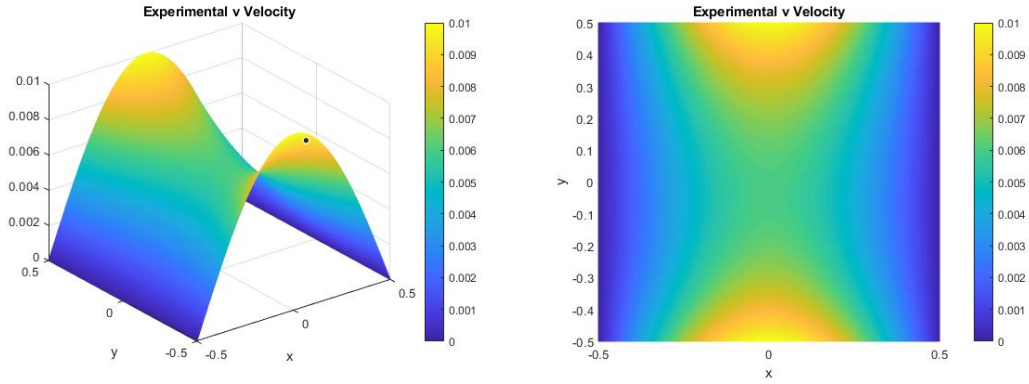

Figure 23: The y-direction velocity v defined over the grid for the experimental boundary condition. This vertical velocity maintains even symmetry in both the x and y directions and reaches a maximum along the top and bottom boundaries.

Based upon these results, we can infer that the fluid moves in a superficially similar fashion to the homogeneous Dirichlet case, but manifests a circulatory movement out of the top of the domain and upward from the bottom of the domain. In the steady-state, this allows for a constant fluid volume within the domain. Accordingly, it may better approximate a physical solution to the governing equations for a free-space

laser-fluid interaction. This is just a single example of an experimental boundary condition, and there are a multitude of possibilities for developing boundary value problems which represent a certain physical setup. In Chapter V, we discuss several alternatives to this approach due to the ambiguity inherent in this procedure.

4.2 Maximum Laser Amplitude

We now reconsider Theorem 4 which described the maximum laser amplitude as an asymptotic of the Re, Ri, Pe numbers. Recall that it stated that if $Re \gg Pe$, then $\varepsilon_{max} = \mathcal{O}\left(Re^{-2}Pe^{-1}Ri^{-1}\right)$ and if $Pe \gg Re$, then $\varepsilon_{max} = \mathcal{O}\left(Re^{-1}Pe^{-2}Ri^{-1}\right)$. Based on these relationships, we expect the maximum allowable amplitude in the numerical iteration to comport with an asymptotic relationship in these parameters. By considering the homogeneous Dirichlet boundary case, we run the algorithm for increasing laser amplitudes until the iteration diverges to determine the max amplitude within an error of 1%. Figures 24 through 28 provide these numerical results as compared to the expected asymptotic relationship.

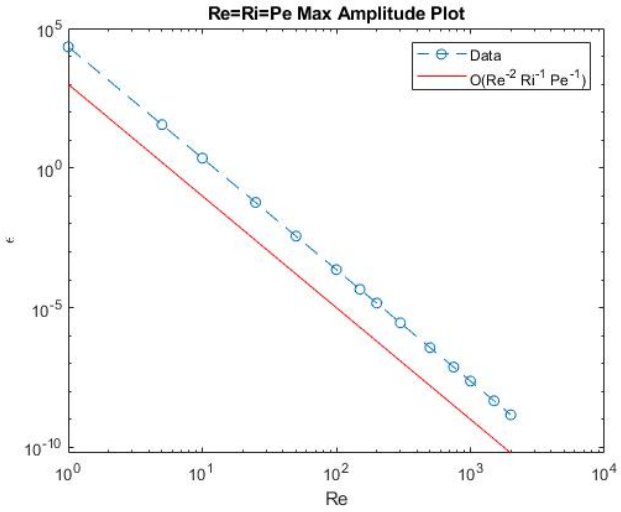

Figure 24: log-log plot of maximum amplitude as a function of $R = Re = Ri = Pe$. Based on the asymptotic relationship, we expect the max amplitude to scale by R^{-4}, which is seen here.

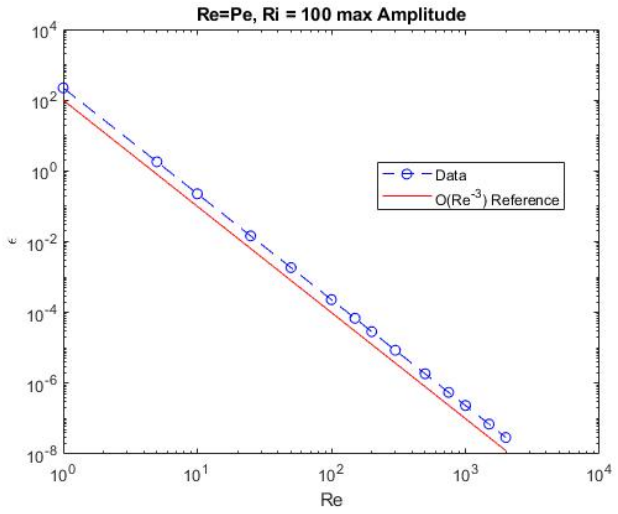

Figure 25: log-log plot of maximum amplitude as a function of $R = Re = Pe$, $Ri = 100$. Based on the asymptotic relationship, we expect the max amplitude to scale by R^{-3}, which is seen here.

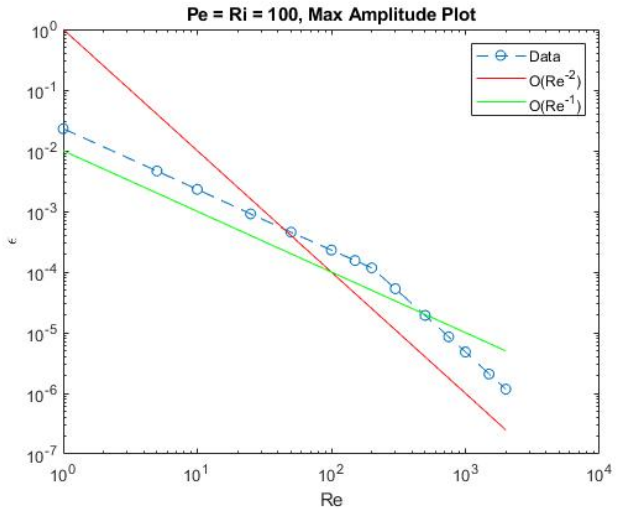

Figure 26: log-log plot of maximum amplitude as a function of Re with $Pe = Ri = 100$. Based on the asymptotic relationship, we expect the max amplitude to scale by Re^{-1} when $Re \ll Pe$ and Re^{-2} when $Re \gg Pe$. This is observed in the plot as the asymptotic relationship changes when $Re \approx Pe$.

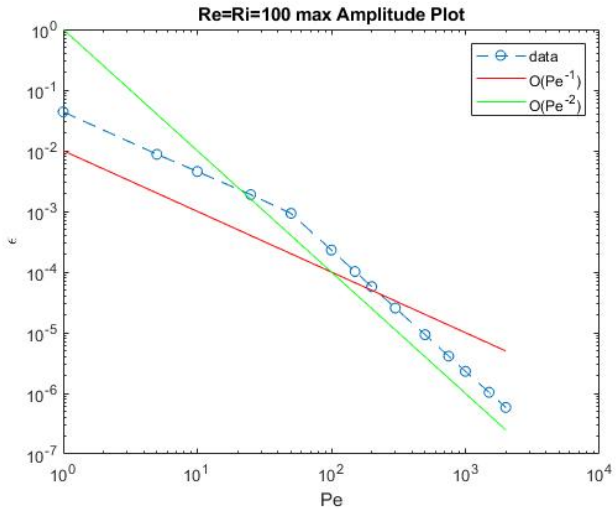

Figure 27: log-log plot of maximum amplitude as a function of Pe with $Re = Ri = 100$. Based on the asymptotic relationship, we expect the max amplitude to scale by Pe^{-1} when $Pe \ll Re$ and Pe^{-2} when $Pe \gg Re$. This is observed in the plot as the asymptotic relationship changes when $Pe \approx Re$.

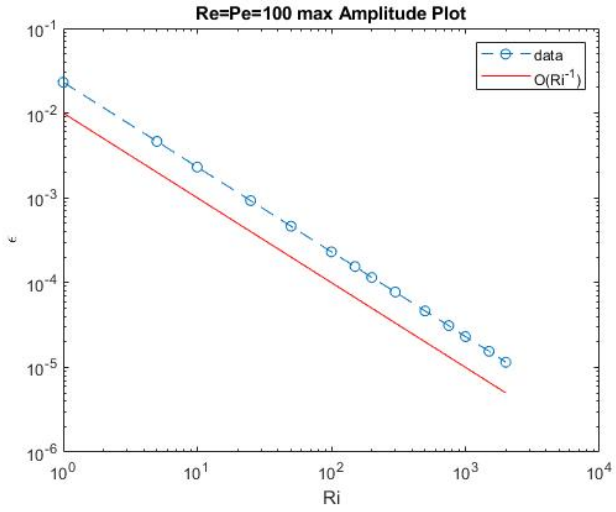

Figure 28: log-log plot of maximum amplitude as a function of Ri with $Re = Pe = 100$. Based on the asymptotic relationship, we expect the max amplitude to scale by Ri^{-1} which is observed in this plot.

From these results, we observe that the convergence analysis performed in Chapter III gives accurate predictions for the maximum laser amplitude as computed in the numerical algorithm. This is significant, since we see that the maximum allowable laser amplitude scales by the inverse square of the Reynolds number or Peclet number depending on their relative size. Hence, finding convergent solutions for both large amplitude laser forcing and large Reynolds and Peclet numbers is very difficult. In the following section, we apply a continuation scheme to see if we can modify the initialization of the algorithm to find solutions at higher laser amplitudes.

4.3 Bifurcation Analysis

Recall that in the proof of Theorem 2 for the existence of steady solutions to the Navier–Stokes equations, we assumed that each fluid variable can be represented as a small perturbation from a resting fluid case on the order of the laser amplitude ε. Further, we showed that these steady solutions are only guaranteed to exist for ε sufficiently small with respect to the domain size and the fluid variables Re, Ri, and Pe. We are therefore interested in determining the amplitude values which allow for a convergent iteration in the fixed-point scheme (39) for fixed Re, Ri, Pe values in a specific boundary value problem. The fluid variables (T, p, u, v) lie within an infinite-dimensional dynamical system as solutions to a system of pdes. Since these solutions represent a steady-state solution to a dynamical system, we may employ a bifurcation analysis to determine how these steady solutions change with respect to different parameters of the system. In this analysis, we restrict our focus to the existence of steady solutions with respect to changes in the laser amplitude ε. By

observing the linearized version of the steady-state Navier–Stokes equations

$$\begin{aligned}
\Delta u &= -Re\frac{\partial p}{\partial x}, && \text{(75a)}\\
\Delta v &= -Re\left(\frac{\partial p}{\partial y} + RiT\right), && \text{(75b)}\\
\Delta p &= -Ri\frac{\partial T}{\partial y}, && \text{(75c)}\\
\Delta T &= -Pe(\varepsilon f), && \text{(75d)}
\end{aligned}$$

we notice that each variable scales with the constant parameters by

$$\begin{aligned}
\|u\|_\infty &\propto \varepsilon ReRiPe, && \text{(76a)}\\
\|v\|_\infty &\propto \varepsilon ReRiPe, && \text{(76b)}\\
\|p\|_\infty &\propto \varepsilon ReRi, && \text{(76c)}\\
\|T\|_\infty &\propto \varepsilon Pe, && \text{(76d)}
\end{aligned}$$

so we seek to find the relationships between ε and $\frac{\|u\|_\infty}{ReRiPe}$, $\frac{\|v\|_\infty}{ReRiPe}$, $\frac{\|p\|_\infty}{ReRi}$, and $\frac{\|T\|_\infty}{Pe}$, respectively. When calculating the numerical solutions in the previous section, we found that the iteration (39) only converged for every boundary case with a sufficiently small $\varepsilon < 10^{-7}$. Due to this phenomenon, we are fundamentally interested in understanding how different initializations come to converge or diverge as ε increases. In the following subsections, we introduce a bifurcation analysis for various boundary value problems including some discussed in the previous section. We employ an adaptive continuation technique to determine solutions for higher ε values, and we compare bifurcation diagrams for the fixed-point iteration and the Newton's method iteration.

4.3.1 Homogeneous Case

We first consider the simplest boundary case of homogeneous Dirichlet on each of the fluid variables. For fixed $Re = Pe = 100$ and $Ri = 1000$ constants, we begin by determining approximately the largest possible ε value such that the initialization (40) converges to a steady solution. This is accomplished by progressively increasing ε until the the iteration diverges for the standard initialization (40). For the constant values defined above, this maximum amplitude took on the value $\varepsilon_{max} \approx 10^{-5}$. Once the standard initialization becomes insufficient to reach convergent solutions, we employ an adaptive continuation scheme. We set $\delta\varepsilon_0 = \varepsilon_{max}$, then check to see if the iteration with amplitude $\varepsilon_{max} + \delta\varepsilon_0$ converges. If so, we assign $\delta\varepsilon = 2\delta\varepsilon_0$. If not, we assign $\delta\varepsilon = \frac{1}{2}\delta\varepsilon_0$ and repeat the process until either the desired amplitude ε^* is reached or the maximum number of continuation steps is met. We perform the same continuation process with Newton's method. Figure 29 provides a bifurcation diagram for the normalized fluid variable norms in relation to the amplitude ε.

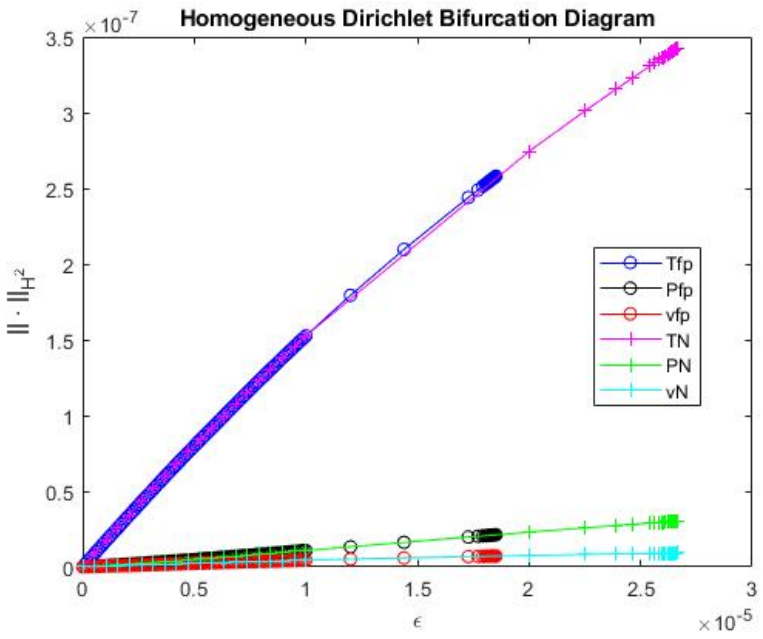

Figure 29: Bifurcation Diagram for Newton's method and the fixed-point iteration with homogeneous Dirichlet boundary conditions. There appears to be a linear relationship between ε and the normalized function norms in this boundary condition. Newton's method is able to continue to slightly higher amplitudes than the fixed-point iteration before reaching a stopping point.

There are three eminent characteristics of this diagram worth exploring. We first note that ε appears to have a linear relationship with the normalized fluid variable norms, suggesting that a small amplitude assumption would work well for this boundary condition. Secondly, we notice that, at the at the conclusion of the adaptive continuation scheme, the buildup of solutions on the bifurcation diagram indicates a stopping point in the dynamical system. This implies that a continuation in the amplitude ε can no longer lead to new solutions. Therefore, we require a more advanced continuation scheme which accounts for the other relationships between parameters. This is unfortunately beyond the scope of this research, but we discuss these implications further in Chapter V. The final component in the bifurcation diagram worth

discussing is that the Newton's method approach was able to continue further in ε than the fixed-point method. While this may suggest algorithmic supremacy, we note that, due to the linearity of the solutions, Newton's method is optimized for finding these kinds of solutions. Therefore, we can solve for amplitudes within the range of the fixed-point solver and then apply a Newton continuation step for larger magnitude ε.

We now consider a bifurcation analysis for the slip boundary condition. By applying the same continuation process described above, Figure 30 provides the bifurcation diagram for the slip condition.

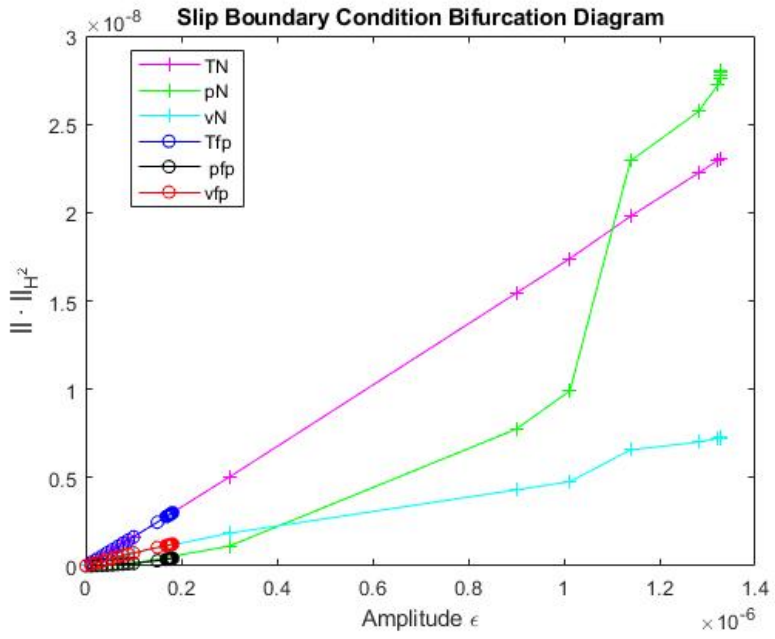

Figure 30: Bifurcation Diagram for Newton's method and the fixed-point iteration with slip boundary conditions. There appears to be a nonlinear relationship between ε and the normalized function norms in this boundary condition as ε grows larger. Newton's method is able to continue to much higher amplitudes than the fixed-point iteration before reaching a stopping point.

We see in this figure that Newton's method converges for much higher amplitudes

than for the fixed-point method. This suggests that the Newton algorithm may be better suited for continuation with homogeneous boundary conditions. As such, we may use the fixed-point solver for lower laser amplitudes and then apply a Newton continuation scheme to solve for larger laser amplitudes if needed.

4.3.2 Inhomogeneous Case

In the previously presented bifurcation diagrams, we considered homogeneous boundary conditions where the Newton solver algorithm was able to continue further than the fixed-point algorithm. We now consider an inhomogeneous boundary condition with represents a partially insulated box. If we suppose that the bottom and side boundaries are insulated and the top boundary is open, then we may represent the temperature and velocity boundary conditions as a mixed type. That is, we assign the top temperature and vertical velocity boundaries to a Dirichlet function, and we assign the normal derivative of the horizontal velocity to be a Neumann function along the top. This boundary condition thus takes the form

$$\begin{cases} T(x,y) = g_T(x), & (x,y) \in \partial\Omega_{\text{top}}, \\ \frac{\partial T}{\partial \mathbf{n}} = 0, & (x,y) \in \partial\Omega_{\text{bottom}} \cup \partial\Omega_{\text{left}} \cup \partial\Omega_{\text{right}}, \\ \frac{\partial u}{\partial y} = h_u(x), & (x,y) \in \partial\Omega_{\text{top}}, \\ \frac{\partial u}{\partial y} = 0, & (x,y) \in \partial\Omega_{\text{bottom}}, \\ u(x,y) = 0, & (x,y) \in \partial\Omega_{\text{left}} \cup \partial\Omega_{\text{right}}, \\ v(x,y) = g_v(x), & (x,y) \in \partial\Omega_{\text{top}}, \\ v(x,y) = 0, & (x,y) \in \partial\Omega_{\text{bottom}}, \\ \frac{\partial v}{\partial x} = 0, & (x,y) \in \partial\Omega_{\text{left}} \cup \partial\Omega_{\text{right}}, \\ P(x,y) = 0, & (x,y) \in \partial\Omega \end{cases} \tag{77}$$

for the functions $g_T(x)$, $h_u(x)$, $g_v(x)$. By picking $g_T(x) = \varepsilon$, $h_u(x) = -\varepsilon ReRixe^{-x^2}$, and $g_v(x) = \varepsilon ReRie^{-x^2}$ for the same constants as in the previous subsection, we apply an adaptive continuation scheme to achieve the bifurcation diagram in Figure 31.

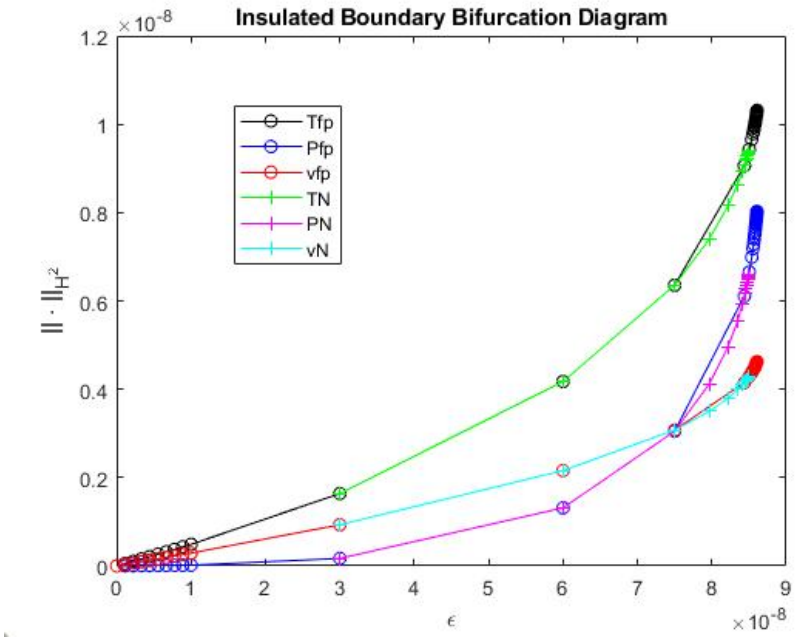

Figure 31: Bifurcation Diagram for Newton's method and the fixed-point iteration with experimental insulated boundary conditions. There is now a nonlinear relationship between the amplitude and the normalized function sizes. The fixed-point method is able to continue to slightly higher amplitudes than the Newton iteration before reaching a stopping point.

From this diagram, we notice immediately that the normalized fluid variable norms take on a nonlinear relationship with ε. This suggests that the interaction between the fluid variables cannot assume a linear model for this specific boundary condition. Moreover, in the bifurcation diagram we notice that the fixed-point iteration can continue further than the Newton iteration in ε. Since Newton's method is optimal for find roots to approximately linear problems, this may indicate that the fixed-point scheme converges more optimally for problems which are nonlinear in nature.

Unfortunately, due to the stopping point, we are unable to explore the majority of the nonlinear regime as ε increases in size. This presents a fundamental roadblock in our pursuit of a methodology which models laser-fluid interaction. Without a more robust continuation scheme, we are left with only finding convergent steady-state solutions for low amplitude laser forcing. In Chapter V, we discuss this phenomenon as it relates to future research opportunities.

V. Conclusions

This research has provided a fixed-point method to numerically solve the 2D steady-state Navier–Stokes equations as approximated by a buoyancy-driven, Boussinesq flow. The necessity of this solution method was driven by the desire to quickly determine the steady-state dynamics of a laser-fluid interaction within a finite domain. By posing the governing equations as a system of coupled, nonlinear Poisson partial differential equations, we introduced a fixed-point iteration which exhibits convergence for small amplitude laser forcing. Within the numerical computation of this iteration, we leveraged the optimal properties of sparse matrix solvers to reduce the overall computational complexity of the algorithm to $\mathcal{O}(N^2 \log N^2)$ for solutions over a discrete grid of size $N \times N$. When compared to a classical Newton solver of complexity at least $\mathcal{O}(N^4)$, this represents a considerable improvement. In pursuit of physically informative solutions, we examined the implementation of various combinations of classical boundary conditions in the Dirichlet, Neumann, and mixed type. Chapter II described the process of determining which boundary conditions would be the most appropriate. In our attempt to model free-space laser-fluid interaction, we found that, due to the nature of the fundamental solution to the Poisson equation in 2D, solutions tend towards infinity as they grow further from the origin. Accordingly, we thus considered only those finite boundary conditions which assume some sort of physical imposition on the fluid dynamics within the domain. When calculating the shape of solutions of these boundary value problems, we found that the boundary construction can drastically change the characteristics of the steady-state fluid flow. With the homogeneous Dirichlet and slip conditions, the streamlines of the steady-state indicated a nearly uniform movement of fluid from the bottom of the domain towards the top. With a careful construction of an experimental boundary condition, however, we were able to generate a steady-state which drove a circulatory motion of

flow into and out of the domain.

By analyzing the convergence properties of the numerical solutions to these boundary value problems, we found that convergent solutions to the iteration only exist for sufficiently small amplitudes ε relative to the flow constants Re, Ri, Pe based on an established asymptotic relationship. The bifurcation analysis of the dynamical system represented by the steady-state solutions to the governing Navier–Stokes equations revealed that convergence properties depended on boundary conditions and chosen iteration schemes. In systems with a more linear relationship between the size of solutions and the amplitude ε, Newton's method was able to continue to higher ε values within the adaptive continuation scheme. Between all the boundary conditions and schemes, however, were the existence of stopping points within the bifurcation analysis of the system. Consequently, we were unable to find steady-state solutions past a certain ε threshold with the current continuation approach. Since these ε thresholds represent a very low-powered laser, the domain of problems which can be physically modeled are severely diminished. Aside from this obstacle, however, we found that the numerical fixed-point method converges asymptotically to steady-state solutions in an especially quick manner. Moreover, in boundary conditions which produce a more nonlinear relationship between ε and the size of solutions, the fixed-point algorithm could continue further than the Newton scheme. From these observations, we've found that we accomplished each research objective outlined in Chapter I especially with regards to the numerical results. We now consider the possibilities of future research to develop the approaches introduced in this thesis.

5.1 Future Work

Throughout the course of developing the necessary theory, methodology, and analysis needed to procure this research, we identified several noteworthy opportunities for

further development in future research. The most prominent findings can be itemized as follows:

- develop an open boundary condition for the fluid domain,
- modify the iteration scheme to fit a 3D problem,
- utilize a more effective continuation scheme to move past stopping points in the Bifurcation diagrams,
- couple fluid solver with an appropriate laser beam propagation model.

When researching the imposition of boundary conditions on the fluid domain Ω, we found that, in an attempt to model circulatory flow of the fluid in and out of the domain, we would have to rely on experimental results to impose boundary conditions which accurately describe the physical nature of the problem. Instead of this approach, it would be beneficial to implement an open boundary condition which allows for fluid movement across the domain. Fornberg [22] and Morrill [15] describe the process of implementing one such boundary condition for a 2D fluid dynamics problem. While this approach will likely produce solutions which are more physically accurate, the computation of the boundary condition itself presents a challenge when we are attempting to develop a scheme which optimizes speed of convergence. Thus, it would be beneficial to research alternative open boundary conditions in the pursuit of finding the most physically accurate solutions while also maintaining the low computational cost of the iteration.

A second ambition for future research is to convert the operation of the fixed-point scheme from a 2D to a 3D domain. Since fluid dynamics fundamentally occur in three dimensions, this approach would be the most useful for characterizing physical phenomena such as thermal blooming. In pursuing this goal, however, the problem of

finding steady-state solutions grows vastly more difficult. Based on the coupling effect of laser interaction with the fluid in a 3D domain, we require an in-depth treatment on the feasibility of converting the fixed-point scheme to run in 3D. By expanding this domain of operations to three dimensions, we are much more likely to find steady-state solutions which lead to useful insights for understanding how lasers influence their surrounding mediums during propagation.

In the bifurcation analysis presented in Chapter IV, we found that we were unable to continue to find steady state solutions past a certain amplitude threshold. This all occurred, however, in a single adaptive continuation scheme solely for the variable ε. In order to move past this stopping point in the bifurcation analysis of the dynamical system, it would be worthwhile to explore alternative continuation schemes such as those presented in Allowgower and Georg [35]. Since this stopping point occurs for rather small ε values, a more versatile continuation scheme may allow us to explore the nonlinear dynamics which occur at high laser forcing amplitudes.

In Chapter II, we imposed the assumption that the laser can be modeled as a 2D Gaussian profile which is represented as an inhomgeneous forcing term in the steady-state Boussinesq Navier–Stokes equations. In a simulation of laser beam propagation, however, it is necessary to model the evolution of the laser in the direction of propagation using a more appropriate physical model. Lax et al. [36] describe a paraxial approximation to Maxwell's equations which may be coupled with a fluid solver in pursuit of a laser-fluid interaction for modeling beam propagation. Going a step further, Deutsch and Garrison [37] establish a quantum version of this paraxial approximation. A multitude of avenues exist by which to couple laser-fluid interactions for propagation; however, it would fruitful to pursue the computation of the steady-state of this laser-fluid interaction with a paraxial laser model. This addition of a laser propagation model, coupled with an expansion in 3D, will allow for greater accuracy

in determining steady-state behavior of laser beam propagation.

Any future research endeavour should be focused on deriving more physically insightful results with respect to the dynamics of laser-fluid interaction. Each of these ambitions provide a conducive means toward achieving that end.

Appendix A. Poisson Solvers Code

Dirichlet Solver:

```
1
2  function [u] = DPsolve(N,f,utop,ubot,uleft,uright)
3
4  % this solves -Del^2 u = -f with dirichlet conditions
5
6
7  if length(utop) ~= length(uleft)
8
9  uleft = [utop(1); uleft; ubot(1)];
10 uright = [utop(end); uright; ubot(end)];
11
12 end
13
14
15 %%% Start direct matrix building approach - let N = N+1 for
       easier matrix
16 %%% building
17 h = 1/N;
18 N = N+1;
19 fvec = reshape(f',N^2,1);
20 bd = zeros(size(f));
21 bd(:,1) = uleft;
22 bd(:,end) = uright;
23 bd(1,:) = utop;
```

```
24 bd(end,:) = ubot;
25 bdvec = reshape(bd',N^2,1);
26
27
28 e0 = ones(N^2,1);
29 e1 = zeros(N^2-1,1);
30 em1 = e1;
31 eN = zeros(N^2-N,1);
32 emN = zeros(N^2-N,1);
33 b = bdvec;
34 for k = 1:N-2
35     e0(k*N+2:k*N+N-1) = 4;
36     b(k*N+2:k*N+N-1) = b(k*N+2:k*N+N-1)-h^2*fvec(k*N+2:k*N+N
           -1);
37     e1(k*N+2:k*N+N-1) = -1;
38     em1(k*N+1:k*N+N-2) = -1;
39     eN(k*N+2:k*N+N-1) = -1;
40     emN((k-1)*N+2:k*N-1) = -1;
41
42 end
43
44 A = spdiags([[emN;zeros(N,1)] [em1;0] e0 [0;e1] [zeros(N,1);
       eN]],[-N,-1,0,1,N],N^2,N^2);
45 I = A\b;
46 u = reshape(I,N,N)';
47
```

```
48 end
```

Neumann Solver:

```
1
2  function [u] = NPsolve(N,f,gtop,gbot,gleft,gright)
3  %This function will solve Poisson with Neumann bcs
4
5  n = N;
6  m = N;
7  h = 1/N; % x step
8  k = 1/N; % y step
9  lam = (h/k)^2;
10 mu = 2*(1+lam);
11 R = (n+1)*(m+1);
12
13 % rhs vector
14 fmat = f;
15 fnvec = reshape(fmat',R,1);
16 bn = zeros(R,1);
17 gmat = zeros(size(fmat));
18 gmat(:,1) = gleft;
19 gmat(:,end) = gright;
20 gmat(1,:) = gtop;
21 gmat(end,:) = gbot;
22 g = reshape(gmat',R,1);
23
24
```

```
25 % main diagonal band
26 e1 = zeros(R,1);
27 e2 = -1*ones(R-1,1);
28 e1([1,n+1,R-n,R]) = 1; % corners
29 bn([1,n+1,R-n,R]) = -1/4*h^2*fnvec([1,n+1,R-n,R]) +h*g([1,n
       +1,R-n,R]);
30 e1([2:n,n+2,R-n-1,(R-n+1:R-1)]) = 2; % top,bottom boundaries
       plus 2 side bd pts
31 bn([2:n,n+2,R-n-1,(R-n+1:R-1)]) = -1/2*h^2*fnvec([2:n,n+2,R-n
       -1,(R-n+1:R-1)]) + h*g([2:n,n+2,R-n-1,(R-n+1:R-1)]); %
       CHANGE TO ACCOUNT FOR TOP/BOT
32 e1(n+3:(2*n+1)) = mu;
33 bn(n+3:(2*n+1)) = -h^2*fnvec(n+3:(2*n+1)); %no g here since
       interior
34 % -1 band
35
36 e2(1:n) = -1/2;
37 e2(R-n:R-1) = -1/2;
38 e2((n+1):(n+1):(R-n)) = 0;
39
40 % -2 band
41 Q = R-n-1;
42 e3 = zeros(Q,1);
43 e3(1) = -1/2;
44 e3(2:n) = -lam;
45
```

```
for j = 1:(m-2)
        e1((j-1)*(n+1)+2*(n-1)+4:(j-1)*(n+1)+2*(n-1)+5) = 2;
        bn((j-1)*(n+1)+2*(n-1)+4:(j-1)*(n+1)+2*(n-1)+5) = -1/2*
            h^2*fnvec((j-1)*(n+1)+2*(n-1)+4:(j-1)*(n+1)+2*(n-1)
            +5)+h*g((j-1)*(n+1)+2*(n-1)+4:(j-1)*(n+1)+2*(n-1)+5)
            ;
        e1((j-1)*(n+1)+2*(n-1)+6:(j-1)*(n+1)+2*(n-1)+6+(n-2)) =
             mu;
        bn((j-1)*(n+1)+2*(n-1)+6:(j-1)*(n+1)+2*(n-1)+6+(n-2)) =
             -h^2*fnvec((j-1)*(n+1)+2*(n-1)+6:(j-1)*(n+1)+2*(n
            -1)+6+(n-2)); % no g here, interior

    e3(j*(n+1):(j*(n+1)+1)) = -1/2;
    e3(j*(n+1)+2:j*(n+1)+2+n-2) = -lam;

end

e3(Q) = -1/2;
e3(Q-n+1:Q-1) = -1;
e3(Q-n) = -1/2;
e3(Q-n-1) = -1/2;


bn = bn-mean(bn); % discrete compatibility condition
An = spdiags([[e3;zeros(R-length(e3),1)] [e2;zeros(R-length(
    e2),1)] e1 [zeros(R-length(e2),1);e2] [zeros(R-length(e3)
```

```
    ,1);e3]],[-(n+1),-1,0,1,(n+1)],R,R);
uvec = An\bn;
u = reshape(uvec,(m+1),(n+1))';

end
```

Slip Solver:

```
function [u] = SPsolvey(N,f,utop)
%This function will solve Poisson with slip conds

n = N;
m = N;
h = 1/N; % x step
k = 1/N; % y step
lam = (h/k)^2;
mu = 2*(1+lam);
R = (n+1)*(m+1);

% rhs vector
fmat = f;
fnvec = reshape(fmat',R,1);
bn = zeros(R,1);
gtop = zeros(R,1);
% go through each row in the matrix
A = zeros(R,R);

```

```
21 for k = [1,n+1,R-n,R]
22 A(k,k) = 1; % four corners
23 end
24 bn(1) = utop(1); % specify dirichlet condition on top corners
25 bn(n+1) = utop(end);
26
27 % A([2:n,(R-n+1:R-1)],[2:n,(R-n+1:R-1)]) = 2; % top,bottom
      boundaries diagonal pts
28
29 for k = 2:n % fill out rest of top, bottom bds
30     A(k,k) = 1;
31     bn(k) = utop(1,k);
32 end
33
34 for k = (R-n+1:R-1)
35      A(k,k) = 1;
36 end
37
38 % A([n+2,R-n-1],[n+2,R-n-1]) = 1; % first left + last right
39
40 A(n+2,n+2) = 2;
41 A(n+2,1) = -1/2;
42 A(n+2,n+3) = -1;
43 A(n+2,2*n+3) = -1/2;
44
45 A(R-n-1,R-n-1) = 2;
```

```
46 A(R-n-1,end) = -1/2;
47 A(R-n-1,R-n-2) = -1;
48 A(R-n-1,R-2*n-2) = -1/2;
49
50 for k = n+3:(2*n+1) % fill out rest of interior
51     A(k,k) = mu;
52     bn(k) = -h^2*fnvec(k);
53     A(k,k-4) = -lam;
54     A(k,k+4) = -lam;
55     A(k,k-1) = -1;
56     A(k,k+1) = -1;
57
58 end
59
60 for j = 1:m-2
61 count = 0;
62 for k = (j-1)*(n+1)+2*(n-1)+4:(j-1)*(n+1)+2*(n-1)+5 % left
       and right
63
64       A(k,k) = 2;
65      bn(k) = -1/2*h^2*fnvec(k);
66      if k - (n+1) > 0
67          A(k,k-(n+1)) = -1/2;
68      end
69
70      if k + (n+1) < R+1
```

```
71          A(k,k+(n+1)) = -1/2;
72      end
73
74      if count == 0
75          A(k,k-1) = -1;
76      else
77          A(k,k+1) = -1;
78      end
79
80      count = count+1;
81
82  end
83
84  for k = (j-1)*(n+1)+2*(n-1)+6:(j-1)*(n+1)+2*(n-1)+6+(n-2)
85      A(k,k) = mu;
86      bn(k) = -h^2*fnvec(k);
87      A(k,k-4) = -lam;
88     A(k,k+4) = -lam;
89     A(k,k-1) = -1;
90     A(k,k+1) = -1;
91  end
92
93  end
94
95  An = sparse(A);
96  uvec = An\bn;
```

```
97
98 u = reshape(uvec,(m+1),(n+1))';
99
100 end
```

Appendix B. Additional Results

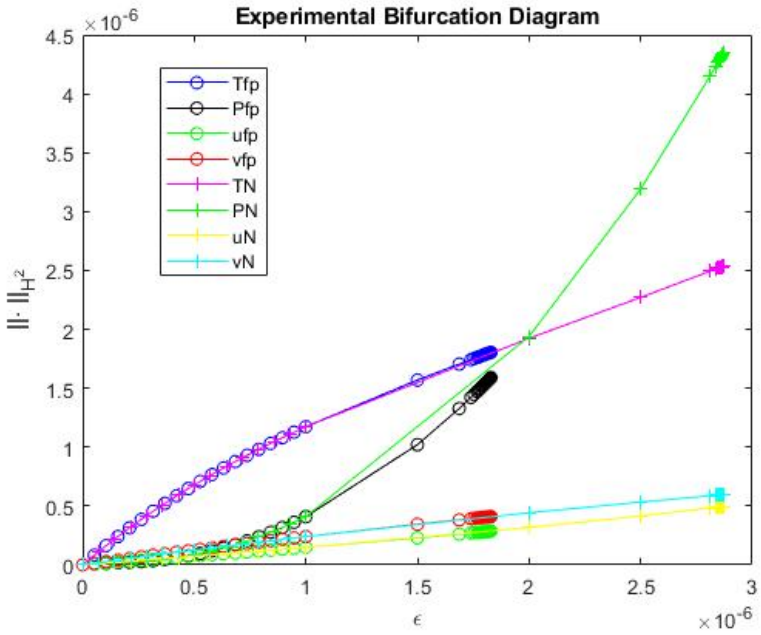

Figure 32: Bifurcation Diagram for Newton's method and the fixed-point iteration with experimental Dirichlet boundary conditions.

Bibliography

1. Frederick G. Gebhardt. High power laser propagation. *Applied Optics*, 15(6):1479, 1976.

2. Raphael Z. Yahel. Turbulence effects on high energy laser beam propagation in the atmosphere. *Applied Optics*, 29(21):3088, 1990.

3. P Sprangle, J R Peñano, A Ting, and B Hafizi. Propagation of High-Energy Lasers in a Maritime Atmosphere. *NRL Review*, pages 59–65, 2004.

4. David C. Smith. High-Power laser Propagation: Thermal Blooming. *Proceedings of the IEEE*, 65, 1977.

5. Phillip Sprangle, Joseph Peñano, and Bahman Hafizi. Optimum wavelength and power for efficient laser propagation in various atmospheric environments. *Journal of Directed Energy*, 2(1):71–95, 2006.

6. Mark F. Spencer. Wave-optics investigation of turbulence thermal blooming interaction: I. Using steady-state simulations. *Optical Engineering*, 59(08):1, 2020.

7. Mark F. Spencer. Wave-optics investigation of turbulence thermal blooming interaction: II. Using time-dependent simulations. *Optical Engineering*, 59(08):1, 2020.

8. Charles L. Fefferman. Existence and smoothness of the Navier-Stokes equation. *The millennium prize problems*, (1):1–5, 2000.

9. S. Prudhomme and J. T. Oden. Numerical stability and error analysis for the incompressible Navier-Stokes equations. *Communications in Numerical Methods in Engineering*, 18(11):779–787, 2002.

10. Rashid A. Ahmad. Steady-state numerical solution of the navier-stokes and energy equations around a horizontal cylinder at moderate reynolds numbers from 100 to 500. *Heat Transfer Engineering*, 17(1):31–81, 1996.

11. S. C.R. Dennis, J. D. Hudson, and N. Smith. Steady laminar forced convection from a circular cylinder at low Reynolds numbers. *Physics of Fluids*, 11(5):933–939, 1968.

12. Simone Deparis and Gianluigi Rozza. Reduced basis method for multi-parameter-dependent steady Navier-Stokes equations: Applications to natural convection in a cavity. *Journal of Computational Physics*, 228(12):4359–4378, 2009.

13. P. M. Livingston. Thermally Induced Modifications of a High Power cw Laser Beam. *Applied Optics*, 10(2):426, 1971.

14. E. Flores-Flores, S. A. Torres-Hurtado, R. Páez, U. Ruiz, G. Beltrán-Pérez, S. L. Neale, J. C. Ramirez-San-Juan, and R. Ramos-García. Trapping and manipulation of microparticles using laser-induced convection currents and photophoresis. *Biomedical Optics Express*, 6(10):4079, 2015.

15. Dana F. Morrill. *Numerical Simulation of High Energy Laser Propagation*. PhD thesis, 2018.

16. David Colton. *Partial Differential Equations*. Dover Publications, INC., New York, 2004.

17. Artem Novozhilov. Green's function for the Poisson equation, 2016.

18. Richard Jozsa. 1B METHODS LECTURE NOTES PART IV : PDEs on unbounded domains, 2011.

19. Stephen D. Fisher. *Complex Variables*. Dover Publications, INC., Mineloa, New York, second ed. edition, 1999.

20. Stephen Hawking. *A Brief History of Time*. Bantam Books, New York, 1992.

21. John D. Anderson. *Fundamental of Aerodynamics*. Fifth ed. edition, 2011.

22. Bengt Fornberg. Steady Viscous Flow Past a Circular Cylinder up to Reynolds Number 600. *Journal of Computational Physics*, 61(2):297–320, 1985.

23. Long Chen. Finite Difference Methods for Poisson Equation, 2019.

24. Arch W. Naylor and George R. Sell. *Linear Operator Theory in Engineering and Science*. Springer-Verlag Inc., New York, second ed. edition, 1982.

25. Haim Brezis. *Functional Analysis, Sobolev Spaces, and Partial Differential Equations*. Springer, 2010.

26. Ethan Y Jaffe. Products in Sobolev Spaces.

27. John Villavert. Elementary Theory and Methods for Elliptic Partial Differential Equations. 2015.

28. Jeffrey Langford. *Comparison Theorems in Elliptic Partial Differential Equations with Neumann Boundary Conditions*. PhD thesis, Washington University, 2012.

29. XinWei Yu. Poisson Equation in Sobolev Spaces, 2011.

30. Harper Langston. 2D Fast Poisson Solver, 2021.

31. The Mathworks Inc. MATLAB Documentation. mldivide.

32. Ake Bjorck. *Numerical Methods in Matrix Computations*. 2015.

33. Kyle A. Novak. *Numerical Methods for Scientific Computing*. 2017.

34. Benjamin F. Akers and Jonah A. Reeger. Numerical simulation of thermal blooming with laser-induced convection. *Journal of Electromagnetic Waves and Applications*, 33(1):96–106, 2019.

35. Eugene L. Allgower and Kurt Georg. *Introduction to numerical continuation methods*. 1990.

36. Melvin Lax, William Louisell, and Wlliam McKnight. From Maxwell to Paraxial Wave Optics. *Physical Review A*, 11(4), 1975.

37. Ivan H. Deutsch and John C. Garrison. Paraxial quantum propagation. *Physical Review A*, 43(5):2498–2513, 1991.

REPORT DOCUMENTATION PAGE

Form Approved
OMB No. 0704–0188

1. REPORT DATE *(DD–MM–YYYY)*	2. REPORT TYPE	3. DATES COVERED *(From — To)*
25–03–2021	Master's Thesis	Sept 2019 — Mar 2021

4. TITLE AND SUBTITLE

A Fixed-Point Method for Computing Steady-State 2D Laser-Fluid Interactions

5a. CONTRACT NUMBER

5b. GRANT NUMBER

5c. PROGRAM ELEMENT NUMBER

6. AUTHOR(S)

2d Lt Jeremiah S. Lane

5d. PROJECT NUMBER

5e. TASK NUMBER

5f. WORK UNIT NUMBER

7. PERFORMING ORGANIZATION NAME(S) AND ADDRESS(ES)

Air Force Institute of Technology
Graduate School of Engineering and Management (AFIT/EN)
2950 Hobson Way
WPAFB OH 45433-7765

8. PERFORMING ORGANIZATION REPORT NUMBER

AFIT-ENC-MS-20-M-002

9. SPONSORING / MONITORING AGENCY NAME(S) AND ADDRESS(ES)

10. SPONSOR/MONITOR'S ACRONYM(S)

11. SPONSOR/MONITOR'S REPORT NUMBER(S)

12. DISTRIBUTION / AVAILABILITY STATEMENT

DISTRIBUTION STATEMENT A:
APPROVED FOR PUBLIC RELEASE; DISTRIBUTION UNLIMITED.

13. SUPPLEMENTARY NOTES

14. ABSTRACT

This research introduces a fixed-point numerical approach for solving the steady-state Navier-Stokes (NS) equations on a finite two-dimensional (2D) domain. The steady-state interaction between a high energy laser beam and its surrounding fluid medium is important to researchers in the field of high energy laser beam propagation. The solutions to the steady-state Navier-Stokes equations provide a model for uncovering the steady-state behavior of the fluid medium, which is useful for the modeling of thermal blooming in laser beam propagation. Numerical solutions remain the only tenable option for solving the NS equations, wherein numerical speed and fidelity beget the utility of any such algorithm. The timing and accuracy results from the novel fixed-point algorithm are compared to a standard Newton solver, where the fixed-point algorithm implements a series of discrete Poisson solvers through successive fixed-point iterations of fluid velocity (u,v), pressure (p), and temperature (T) in a Boussinesq fluid model. The fixed-point scheme consistently proves superior in computational cost by converging after $\mathcal{O}(N^2 \log N^2)$ flops compared to the $\mathcal{O}(N^6)$ flops in the Newton Solver for a discrete $N \times N$ grid. We provide a proof for the convergence of small amplitude solutions, and discuss the relationship between fluid parameters (Re, Ri, Pe) and the existence of solutions as a function of laser intensity in a bifurcation analysis.

15. SUBJECT TERMS

Navier–Stokes, Thermal Blooming, Fixed-Point Algorithm

16. SECURITY CLASSIFICATION OF:			17. LIMITATION OF ABSTRACT	18. NUMBER OF PAGES	19a. NAME OF RESPONSIBLE PERSON
a. REPORT	b. ABSTRACT	c. THIS PAGE			Dr Benjamin J. Akers, AFIT/ENC
U	U	U	UU	103	19b. TELEPHONE NUMBER *(include area code)* (937) 255-3636; benjamin.akers@afit.edu